AGU PUBLICATIONS

JGR

Journal of Geophysical Research: Atmospheres

RESEARCH ARTICLE
10.1002/2016JD025131

Key Points:
- Vertical profile of volcanic ash emissions can be estimated accurately by assimilating satellite data and ground-based observations
- Volcanic ash forecast is significantly improved due to the accurate estimate of emission
- Guidance on preprocessing and properly use of satellite observations is provided

Supporting Information:
- Data Set S1
- Data Set S2
- Data Set S3

Correspondence to:
S. Lu,
S.Lu-1@tudelft.nl

Citation:
Lu, S., H. X. Lin, A. Heemink, A. Segers, and G. Fu (2016), Estimation of volcanic ash emissions through assimilating satellite data and ground-based observations, *J. Geophys. Res. Atmos.*, *121*, 10,971–10,994, doi:10.1002/2016JD025131.

Received 23 MAR 2016
Accepted 12 SEP 2016
Accepted article online 21 SEP 2016
Published online 28 SEP 2016

Estimation of volcanic ash emissions through assimilating satellite data and ground-based observations

Sha Lu[1], Hai Xiang Lin[1], Arnold Heemink[1], Arjo Segers[2], and Guangliang Fu[1]

[1]Delft Institute of Applied Mathematics, Delft University of Technology, Delft, Netherlands, [2]Department of Climate, Air and Sustainability, TNO, Utrecht, Netherlands

Abstract In this paper, we reconstruct the vertical profile of volcanic ash emissions by assimilating satellite data and ground-based observations using a modified trajectory-based 4D-Var (Trj4DVar) approach. In our previous work, we found that the lack of vertical resolution in satellite ash column data can result in a poor estimation of the injection layer where the ash is emitted into the atmosphere. The injection layer is crucial for the forecast of volcanic ash clouds. To improve estimation, Trj4DVar was implemented, and it has shown increased performance in twin experiments using synthetic observations. However, there are some cases with real satellite data where Trj4DVar has difficulty in obtaining an accurate estimation of the injection layer. To remedy this, we propose a modification of Trj4DVar, test it with synthetic twin experiments, and evaluate real data performance. The results show that the modified Trj4DVar is able to accurately estimate the injection height (location of the maximal emission rate) by incorporating the plume height (top of the ash plume) and mass eruption rate data obtained from ground-based observations near the source into the assimilation system. This will produce more accurate emission estimations and more reliable forecasts of volcanic ash clouds. Also provided are two strategies on the preprocessing and proper use of satellite data.

1. Introduction

Volcanic eruptions release a large amount of volcanic ash, which poses a hazard on human and animal health, land transportation, and aviation safety [*Casadevall*, 1994; *Horwell and Baxter*, 2006; *Fu et al.*, 2016a]. Therefore, hazard assessment and operational volcano monitoring are necessary to provide advisory information and timely volcanic ash forecasts. In order to obtain reliable model predictions, along with validated atmospheric transport models capable of modeling volcanic ash transport and dispersion processes, accurate estimations of emission source terms are required. However, source parameters, such as the total emission rate, the injection height, and the vertical distribution of the emission rate, are poorly known and pose a great challenge to accurate estimation.

Indirect methods have been used to estimate volcanic ash emissions for predictive purposes [*Mastin et al.*, 2009]. Plume height can be obtained from aircraft measurements [*Mankin et al.*, 1992] or ground-based radar and lidar observations [*Wang et al.*, 2008]. Eruption rate can be determined using an empirical relationship between plume height above the vent and total volume [*Mastin et al.*, 2009]. Emission plume can be computed combining the plume height, eruption rate, and a presumed vertical distribution. However, this approach is not always feasible. First, the plume height observations are often not available, and second, the empirical relationship is loose. Furthermore, one of the main limitations of this approach is that it does not provide an estimate for the vertical distribution of the emissions, which can vary substantially. *Mastin et al.* [2009] also provide estimates of the fraction of total emitted mass carried by small particles (< 63 μm diameter), which is termed as "fine ash fraction." These fine particles are known to be able to survive early fall out near the source [*Rose et al.*, 2001]. A limitation of using this fine ash fraction is that the fraction values can vary a lot ranging from 2% to 60% depending on the type of volcano, and the assumption on this strongly affects the forecasts of fine ash.

Data assimilation (DA) techniques, which have been used in traditional weather forecasting for many years, can be applied for forecasting volcanic ash [*Fu et al.*, 2016b]. Automated calibration through DA combines models with observations to produce improved model parameters. There are two main categories of modern DA, filtering [*Evensen*, 1994] and variational methods [*Le Dimet and Talagrand*, 1986]. The former is a class

of sequential methods based on Bayesian formalism. The latter solves for an optimal set of parameters by minimizing a cost function that measures the difference between the model outputs and the observations [*Strunk et al.*, 2010]. The variational approach has already been used to estimate volcanic eruptive parameters and to improve the forecast accuracy using satellite Ash Mass Loading (AML) data. *Flemming and Inness* [2013] used satellite observations of sulfur dioxide to estimate the total emission rate and plume height using a "trajectory-matching" 4D-Var method. However, the vertical distribution of the emission rate remained uncertain. *Eckhardt et al.* [2008] first reconstructed the vertical profiles of sulfur emissions from AML data based on the inverse modeling approach proposed by *Seibert* [2000]. *Stohl et al.* [2011] improved the inverse modeling method to estimate the vertical profile of the volcanic ash emissions and the mass eruption rate of fine ash as a function of both height and time. *Lu et al.* [2016] introduced a trajectory-based 4D-Var (Trj4DVar) approach for the reconstruction of the vertical profile of volcanic eruptions.

In our previous study [*Lu et al.*, 2016], we conducted twin experiments with synthetic observations of ash columns to estimate volcanic ash emissions. It was demonstrated that standard 4DVar was not able to reconstruct the vertical profile of the emissions or to determine the injection height. Failure is attributed to the lack of vertical information in AML data. Hence, the Trj4DVar was proposed and tested in twin experiments. It showed good performance and great potential to be used with real satellite data.

Based on experimental outcomes, we concluded that Trj4DVar is able to reconstruct the vertical profile within large assimilation windows (>6 h). However, there are cases utilizing real satellite data in which Trj4DVar fails to determine the injection height accurately. This is caused by the estimation problem being ill conditioned in combination with the large uncertainty of satellite data. Using only AMLs appears to be insufficient for reliable forecast results, and Trj4DVar has to be adapted to integrate other observations.

Information about the plume height (PH) and the mass eruption rate (MER) are available for some extensively monitored volcanoes from ground-based, airborne, and spaceborne measurements. PH can be observed from the ground by weather radar, Lidar, and webcam [*Lacasse et al.*, 2004; *Arason et al.*, 2011; *Mona et al.*, 2012; *Flentje et al.*, 2010; *Ansmann et al.*, 2010]. Aircrafts and weather balloons have provided in situ measurements of PH with high temporal resolution and accuracy [*Weber et al.*, 2012; *Petäjä et al.*, 2012]. For unmonitored or hardly accessible volcanoes, one still has to rely on satellite data. *Zakšek et al.* [2013] have recently developed a photogrammetric method to determine the height of the volcanic ash cloud through simultaneous retrieval of optical data from polar orbiting and geostationary satellites. In addition, the trajectory-matching method in *Flemming and Inness* [2013] can be used to automatically estimate injection height and MER as a part of the DA process. This provides a new possibility to increase the accuracy of estimation results by integrating the information of PH and MER into DA systems.

In this study, we propose a modification of the trajectory-based 4D-Var (Trj4DVar) approach in order to be able to estimate emission rates using a combination of satellite ash mass loading data and information of PH and MER. Twin experiments are designed based on the eruption activity of Eyjafjallajökull in April 2010 to test the performance of Trj4DVar and the impact of the use of the additional information (PH and MER). We apply this modified approach to a realistic case with real satellite ash column data, obtained from Spinning Enhanced Visible and Infrared Imager (SEVIRI) instruments. Instead of fine ash fraction, we use the Satellite-Constraint Ash Fraction (SCAF) which defines the emitted mass fraction carried by the particles with radii ranging from 1 μm to 16 μm constrained by SEVIRI retrievals. Studies show that very fine particles (<30μm diameter) with extended atmospheric residence present the greatest hazard [*Rose and Durant*, 2009]. Therefore, the SCAF in this case is also good to simulate the distal part of the ash cloud (>500 km from the source or >6 h travel time) in long-range forecasts [*Dacre et al.*, 2013]. Satellite data should be used carefully. The data have a large uncertainty resulted from retrieval noise, and ash may be undetected or wrongly detected due to erroneous meteorological conditions. Therefore, we also present some guidance for preprocessing satellite data in order to achieve more accurate forecasts.

The paper is organized as follows: In section 2 we introduce the Trj4DVar approach and two heuristic modifications to include PH and MER. In section 3 we give a brief description of AML data, PH, and MER information that are used in the experiments. Section 4 provides a sketch of the volcanic ash transport model, LOTOS-EUROS. Section 5 depicts the twin experiment with synthetic observations and an experiment with the observations described in section 3. In section 6 SEVIRI data and ground-based observations are used for the estimation of volcanic ash emissions. In section 7 the conclusions of this study are summarized.

2. Assimilation Methodology

2.1. Model Representation

The volcanic ash transport process can be mathematically represented as follows:

$$\boldsymbol{x}_k = \mathcal{M}_k(\boldsymbol{x}_{k-1}, \boldsymbol{u}_k + \boldsymbol{\omega}_k), \tag{1}$$

$$\boldsymbol{y}_k = \mathcal{H}_k(\boldsymbol{x}_k) + \boldsymbol{\gamma}_k. \tag{2}$$

where $\mathcal{M}_k$ represents the volcanic ash transport model (LOTOS-EUROS, see section 4) operator for the time evolution from time t_{k-1} to t_k. $\boldsymbol{x}_k \in \mathbb{R}^n$ is the 3-D state vector which contains ash concentrations or aerosol mixing ratios produced by LOTOS-EUROS simulations. $\boldsymbol{u}_k \in \mathbb{R}^p$ is the volcanic ash emission rate in a column as input to the model, which comprises the emission rates at p vertical layers over the summit.

$\mathcal{H}_k$ is the observational operator, which transforms the ash concentrations (model products) to AMLs (satellite retrievals or other observations). $\boldsymbol{y}_k \in \mathbb{R}^n$ contains the observations. In the field data experiment, $\mathcal{H}_k$ is used with a mask matrix to calculate the AMLs at grid cells where ash is detected. In practice, some grid cell ash retrievals bear large uncertainties. The data in those pixels will disturb the assimilation process and should be excluded. A mask matrix is therefore applied to screen out the grid cells where the data are unusable.

The noise terms $\boldsymbol{\omega}_k$ and $\boldsymbol{\gamma}_k$ represent the model and observation uncertainty, respectively, both in terms of a Gaussian distribution with covariance matrices $\mathbf{B}_k$ and $\mathbf{R}_k$, respectively. The model uncertainty is assumed to be in the input $\boldsymbol{u}_k$. Parameterizations of $\mathbf{B}_k$ and $\mathbf{R}_k$ are discussed in section 5.1.

2.2. Incorporating Mass Loading and Plume Height Information in Trj4DVar

Lu et al. [2016] proposed a trajectory-based 4D-Var (Trj4DVar) to estimate emission rates from ash mass loadings based on the concept of 4D-Var and a trajectory-matching approach. Trj4DVar seeks an optimal linear combination of trajectories generated with different inputs (emission) to fit the observation data as good as possible, by minimizing a reformulated 4D-Var cost function as follows:

$$\begin{aligned} J(\boldsymbol{\beta}) &= \frac{1}{2}\sum_{k=1}^{Nt}\left(\sum_{i=1}^{p}\beta^i\Delta\boldsymbol{y}_k^i + \boldsymbol{y}_k^0 - \boldsymbol{y}_k\right)^T[\mathbf{R}_k]^{-1}\left(\sum_{i=1}^{p}\beta^i\Delta\boldsymbol{y}_k^i + \boldsymbol{y}_k^0 - \boldsymbol{y}_k\right) \\ &+ \frac{1}{2}\left(\boldsymbol{u}-\boldsymbol{u}^b\right)^T[\mathbf{B}_k]^{-1}\left(\boldsymbol{u}-\boldsymbol{u}^b\right) \\ &= J^o + J^b, \end{aligned} \tag{3}$$

where $\boldsymbol{\beta} = [\beta^1, \cdots, \beta^p]$ is the vector of coefficients for the linear combination of the trajectories $\Delta\boldsymbol{y}_k^i$, J^o and J^b represent the observation term and the background term, respectively. Further details can be found in the appendix.

In an ideal situation, with a perfect model and exact observations, Trj4DVar can accurately estimate the parameters; however, it encounters difficulty in dealing with real satellite data with a large uncertainty. In this work, we propose two schemes of integrating the additional information of PH and the MER in the DA process to enhance the estimates. The idea is to restrict the sum of emission rates at all layers to the value of MER and the maximal emission rate to be at the injection layer. The injection layer is calculated with observations of the PH. The two modifications are defined as follows:

1. Penalty term correction: Add penalty terms containing additional information to the cost function:

$$J(\boldsymbol{\beta}) = J^o + J^b + J^p, \tag{4}$$

where J^o and J^b are defined in equation (A5) in the appendix. The penalty term J^p restricts most of the emission products to the injection layer and restricts the MER to the observations (such as the satellite mass loadings). For instance, in the twin experiment of this paper, we compute the total mass loading from satellite retrievals (summation of mass loadings at all pixels) at the beginning of the assimilation time m_0 and at the end of the assimilation time is m_{Nt}. The Satellite-Constraint MER can now be roughly calculated as follows:

$$\mathrm{MER} = \frac{m_{Nt} - m_0}{t_N - t_0}. \tag{5}$$

We require a fraction f_m of this MER distributed at the injection layer indexed by i_h and require the summation along the emission column $\boldsymbol{u}$ equal MER as follows:

$$J^p(\boldsymbol{\beta}) = \alpha_h \left(\boldsymbol{u}^T \boldsymbol{e}_{i_h} - f_m * \mathrm{MER}\right)^2 + \alpha_m \left(\boldsymbol{u}^T \boldsymbol{\epsilon} - \mathrm{MER}\right)^2, \tag{6}$$

where α_h and α_m are weight factors, the unit vector $\boldsymbol{e}_i$ is a vector with the ith element equals 1, all others are 0, and $\boldsymbol{\epsilon}$ is a vector filled with ones. Note that the calculation of MER (5) does not take removal processes (such as sedimentation) into account. A better MER can be achieved by using a combination of satellite observations and other types of observations. This MER is constrained by the limitations of satellite retrieval of ash to a certain size range within the Satellite-Constraint Ash Fraction (SCAF). In order to obtain a reasonable model forecast after the assimilation, the emitted MER including all particle sizes should be corrected by the SCAF.

2. Background term correction: Generate a new emission based on the additional information and substitute it for the background

$$J(\boldsymbol{\beta}) = J^o + \alpha_b \left(\boldsymbol{u} - \boldsymbol{u}^{b,\mathrm{new}}\right)^T \left[\mathbf{B}^{\mathrm{new}}\right]^{-1} \left(\boldsymbol{u} - \boldsymbol{u}^{b,\mathrm{new}}\right) = J^o + J^{b,\mathrm{new}}, \tag{7}$$

where $\boldsymbol{u}^{b,\mathrm{new}}$ is calculated according to the additional information of PH and MER with a predefined vertical distribution. The new error covariance matrix $\mathbf{B}^{\mathrm{new}}$ represents the uncertainty of $\boldsymbol{u}^{b,\mathrm{new}}$ that should be smaller than $\mathbf{B}_k$. The vertical distribution could be based on explicit assumptions, such as uniform-distributed [*Dacre et al.*, 2011], umbrella-shaped [*Stuefer et al.*, 2013; *Webley et al.*, 2012], Poisson-distributed, exponentially distributed plume [*Searcy et al.*, 1998], or based on characteristics of the current eruption type.

Note that the maximal of emission rate does not necessarily cover only one layer depending on the vertical extent. Therefore, the injection layer in the two modifications should be extended to multiple layers according to the observations. Besides, the background term J^b in the formula of the penalty term correction (4) can also be replaced by $J^{b,\mathrm{new}}$ in formula (7). In the experiments, the original J^b is used to include the influence of a priori information since the injection height value is uncertain as mentioned in section 3.2.

In order to determine the weight factors α_m, α_h, and α_b, two schemes are considered as following. One is based on the uncertainty of the additional information, and the weight factors are chosen as follows:

$$\alpha_m = c1_m, \quad \alpha_h = c1_h, \quad \alpha_b = c1_b. \tag{8}$$

where $c1_m$, $c1_h$, and $c1_b$ are constants. The other is based on the accumulative influence of the uncertainty in each time step; thus, the weight factors are linearly related to the length of assimilation window as

$$\alpha_m = c2_m * Nt, \quad \alpha_h = c2_h * Nt, \quad \alpha_b = c2_b * Nt, \tag{9}$$

where $c2_m$, $c2_h$, and $c2_b$ are constants.

3. Observations for Assimilation

We use the Eyjafjallajökull 2010 volcanic eruption event as a case study. The 39 day long eruption in April–May 2010 resulted in a dispersal of ash over a large part of Europe. It caused unprecedented disruption to air traffic, and its implications on modern society have made Eyjafjallajökull 2010 a landmark event. Various techniques and observations have been used to detect the volcanic ash cloud and provide unique data for various studies. In this study, we focus on the first explosive phase, 14–18 April.

3.1. SEVIRI Ash Mass Loading Data

Spinning Enhanced Visible and Infrared Imager (SEVIRI) [*Schmetz et al.*, 2002] is a 12-channel spin-stabilized imaging radiometer aboard the Meteosat Second Generation platform, in geosynchronous orbit situated approximately over 0° longitude and 0° latitude. The total field of view coverage of the Earth's surface and atmosphere is 70° from 70°S to 70°N and 70°W to 70°E. Measurements are made of spectral range from visible (500 nm) to the infrared (13,400 nm) with a spatial resolution of 3 km × 3 km at the subsatellite point and 10 km × 10 km at the edge of the scan. Images can be acquired in all channels for the whole of the 70° disk every 15 min.

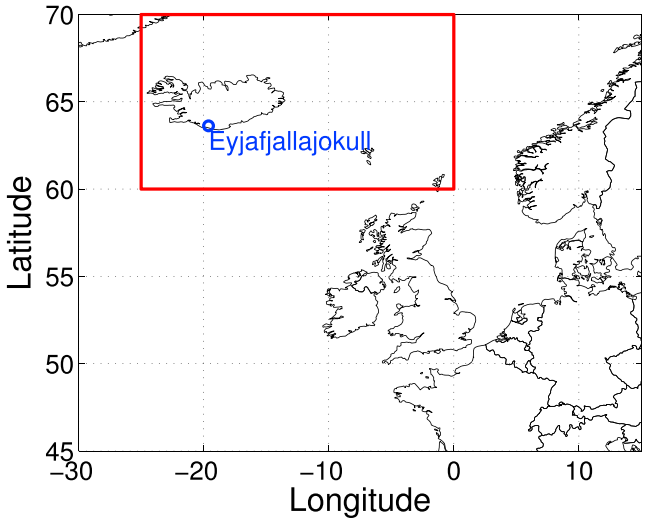

Figure 1. Simulation domains of European area for prediction and Iceland area within the red box for assimilation.

Prata and Prata [2012] retrieved the ash mass loadings (AMLs) based on infrared channels for the case study of Eyjafjallajökull in a subregion of the disk covering 40°N to 70°N and 30°W to 30°E. This region includes the geographic area affected by the Eyjafjallajökull volcanic ash. The data products from the SEVIRI ash retrievals contain estimates of mass loadings of particles with radii between 1 μm and 16 μm, the effective particle radius, and the retrieval errors in mass loadings at ash-detected pixels. In the Eyjafjallajökull data set, 15 min samples were provided starting on 14 April 2010, 00:00 UTC and ending on 22 May 2010, 23:45 UTC. The 15 min pixel-by-pixel mass loadings were then binned into 0.1° × 0.1° grid cells and time-averaged every hour. A parallax correction [*Vicente et al.*, 2002] was applied to all ash-detected pixels by first assuming that the ash clouds were at 6 km height. This simplification introduces a small error in geolocation but is an improvement compared to using the data without a parallax correction. The data are the same as used by *Stohl et al.* [2011].

In our study, the data in the European continental domain (Figure 1) are used for validation, while the data in the region of Iceland (area within the red box of Figure 1) are used for the assimilation. The Iceland domain includes the area affected by the ash released within 6 h, which is the maximal length of the assimilation window in our experiments.

3.2. Additional Information of PH and MER

The height of the plume was monitored every 5 min with a weather radar located in Keflavík International Airport, at 155 km distance from the volcano. The radar was the only operational weather radar in Iceland during the eruption, which gave operational doppler scans from the beginning of the eruption toward the end of April. In case of a volcanic eruption within a radius of 240 km from the radar, the scanning strategy is to make 240 km reflectivity scans every 5 min (except at 5 and 35 min past the hour when 120 km doppler scans are made). Plume height (echo top altitude) is calculated from the volume reflectivity data with a lowest-altitude limitation of 2.9 km, which is archived at the Icelandic Meteorological Office (IMO). Figure 2a shows the time series and the 6 h averages constructed from the radar detected echo tops by IMO, taken from *Arason et al.* [2011]. These PH data will be used in the twin experiment in section 5. Additionally, *Gudmundsson et al.* [2012] provided the 6-hourly mean and maximum values of the plume altitude based on Keflavík radar observations (Figure 2b, top), which will be used in the field data experiment in section 6.

Mass eruption rate information was reported by *Gudmundsson et al.* [2012], shown in the Figure 2b (bottom), and this MER data will be used in field data experiment in section 6. The magma discharges were produced from combining information from tephra fallout maps and PH variations with time. The total volume for different periods is obtained from isopach maps on land and piecewise exponential decline outside Iceland. *Gudmundsson et al.* [2012] computed the 6-hourly discharge rate by applying the record of the PH to a scaled version of the empirical formula of *Mastin et al.* [2009]:

$$Q_i = 0.0564 k_i \left[\frac{H_{\text{med}} + H_{\text{max}}}{2}\right]^{4.15}. \tag{10}$$

Here Q_i ($m^3\ s^{-1}$) is the average magma discharge for the 6 h interval. H_{med} and H_{max} are, respectively, the median and maximum values of the plume height over the vent for the interval. k_i is the scaling factor tuned in such a way that when integrated, it yields values that fit the total ash volume estimates.

Note that the radar-observed PH value is not necessarily the injection height of the fine particles to be assimilated because the PH data bears a 20% uncertainty [*Bonadonna and Costa*, 2013]. Microwave radar echoes

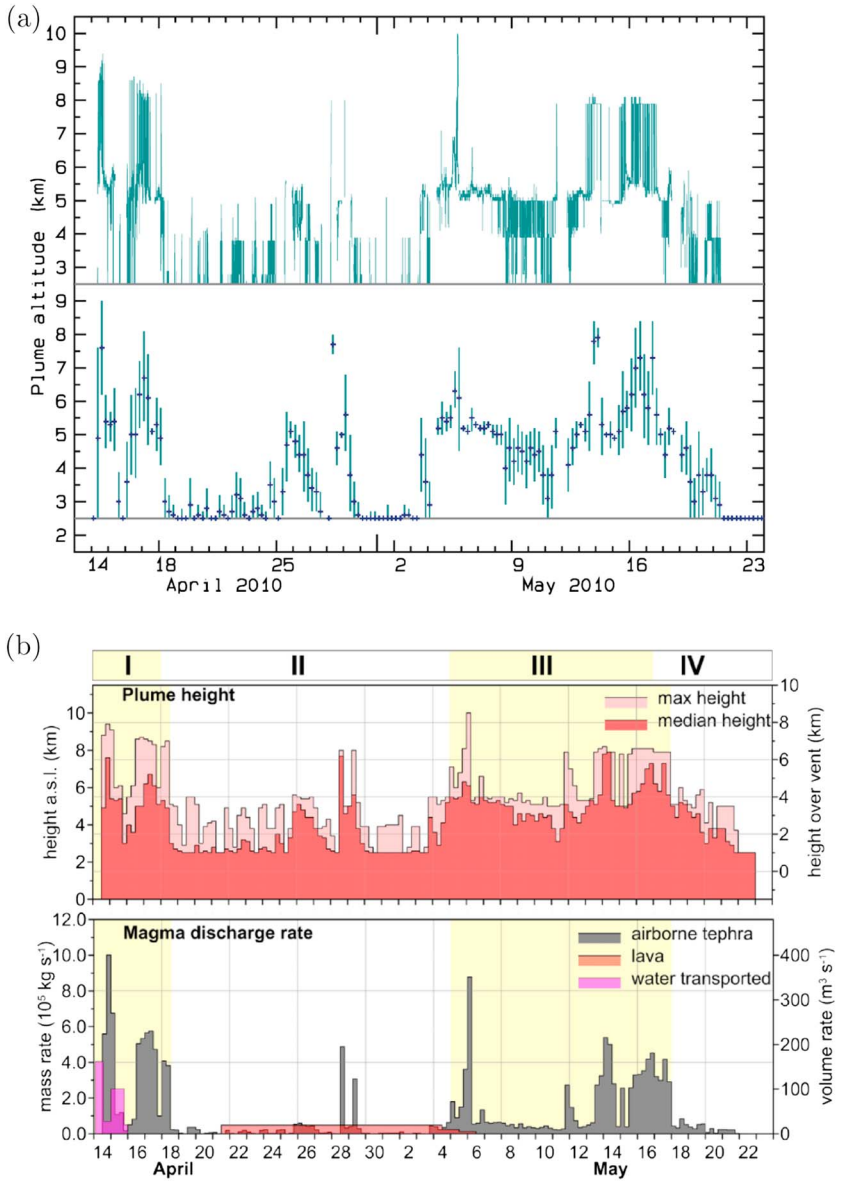

Figure 2. Additional information of (a) plume height obtained from a weather radar used for the twin experiment, taken from *Arason et al.* [2011] and (b) eruption source parameters used for the field data experiment, taken from *Gudmundsson et al.* [2012]. The 5 min time series of the echo top radar data of the eruption plume altitude (km) (Figure 2a, top). The 6 h averages of the echo top heights of the eruption plumes (km) with the bars representing the standard deviation (Figure 2a, bottom). Six hourly mean and maximum values of the plume altitude based on the weather radar in Keflavík (Figure 2b, top). Magma discharge based on combining plume and tephra dispersal data (Figure 2b, bottom).

are sensitive to coarse ash and lapilli concentrations (with size range from 2 to 64 mm in diameter) but not necessarily to moderate and light (< 5 g m^{-3}) fine ash distributions [*Marzano et al.*, 2011]. Moreover, radar observes ash plume top height, which may not be where the maximal emission rate locates, leading to further inaccuracies.

4. Volcanic Ash Modeling

To simulate transport and dispersion of volcanic ash, a deterministic aerosol transport model, the LOTOS-EUROS (version 1.10), is employed in this study. We used a PC with an Intel Xeon E3-1240 V2 processor with 8 cores, a total memory of 32 GB (approximately 5% was taken during experiments) and a clock speed of 3.4 GHz. The LOTOS-EUROS model [*Schaap et al.*, 2008] is an operational air-quality model, used for daily air-quality

Table 1. Input Parameters for 14–19 April 2010 Period of Activity at Eyjafjallajökull [*Webley et al.*, 2012]

Start Time (UTC)	Duration (Hour)	Height (km asl)	Eruption Rate (m^3 s^{-1})	Eruption Rate (kg s^{-1})
4/14/2010 09:00	10	9	219.553	5.71E+05
4/14/2010 19:00	9	5.5	14.884	3.87E+04
4/15/2010 04:00	39	6	199.503	6.44E+04
4/16/2010 19:00	35	8.25	140.325	3.65E+05
4/18/2010 06:00	17	5	8.335	2.17E+04
4/18/2010 23:00	1	4	1.898	4.93E+03

forecasts over Europe [*Curier et al.*, 2012], focusing on ozone, nitrogen oxides, and particular matter. Recently, it has been extended and tested for modeling volcanic ash plumes by *Fu et al.* [2015]. This model accounts for the advective and diffusive transport, sedimentation, and wet and drydeposition, ignoring coagulation, evaporation, and resuspension processes.

The model is driven by 3-D meteorological fields from the European Centre for Medium-Range Weather Forecasts, which are updated every 3 h and are interpolated to an hourly resolution with 0.5° × 0.25° spatial resolution. The model has 12 vertical layers using a dynamic mixing layer approach to determine the model vertical structure [*Schaap et al.*, 2008] in the model domain (45° to 70° north and 30° west to 15° east). Ash concentrations are computed hourly with a priori emissions as input to the model for the first phase (explosive) of the eruptive activity of Eyjafjallajökull event on 14–18 April 2010.

A priori emissions are given in an eruption column over the summit, determined by the eruption source parameters of PH, MER, vertical distribution (VD) and particle size distribution (PSD). PH is obtained hourly from the Icelandic Meteorologic office (IMO) based on radar data and pilot observations (Figure 2a). MER is calculated from PH according to empirical relationship:

$$H = 0.365M^{0.225}, \tag{11}$$

where H (km) is the plume height above the volcano summit and M (kg s^{-1}) represents the MER given by *Dacre et al.* [2011], which was originally reported by *Leadbetter and Hort* [2011]. The information on PH and MER are shown in Table 1. This information has originally been used by *Webley et al.* [2012] as input for the Weather Research and Forecasting-Chem model. The vertical emission profile is then computed from PH, MER, and a typical "umbrella"-shaped VD. We use the same PSD as defined in *Fu et al.* [2015], where six tracers are categorized by the radius of the particles (see Table 2). These tracers are simulated independently with different sedimentation mechanisms.

5. Twin Experiments and Discussion

Twin experiments are designed to test the performance of the Trj4DVar approach and the impact of integrating the injection height and the total mass loading in the DA system. The experiments are carried out using the Eyjafjallajökull 2010 eruptive event as a case study.

5.1. Experimental Setup

In the twin experiments, we estimate the emission rates from the background emissions and the observations. The synthetic observations are generated hourly by summing up the mass loadings of all the six tracers in

Table 2. Volcanic Ash Particle Size Distribution and Ash Bins Property for LOTOS-EUROS Model Simulation[a]

Bins	Particle Diameter (μm)	Mass Fraction (%)	Average Particle Size (μm)
Vash_1	250 to 2000	29	1125.00
Vash_2	63 to 250	31	156.50
Vash_3	30 to 63	12	46.50
Vash_4	10 to 30	18	20.00
Vash_5	2.5 to 10	8	6.25
Vash_6	0.0 to 2.5	2	1.25

[a]Ash particles categorized in vash_4 to vash_6 are constrained by SEVIRI retrievals and are used to compare model simulations and satellite observations.

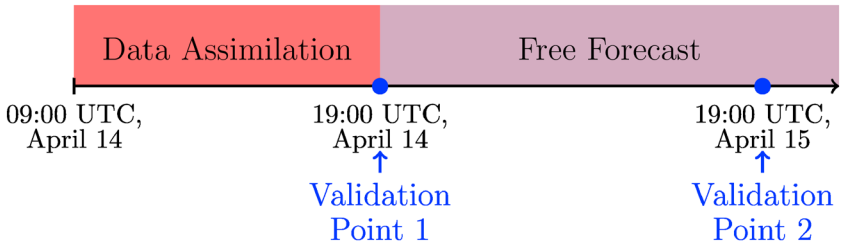

Figure 3. Timeline of the twin experiment.

Table 2 from the "true" ash concentrations. These ash concentrations are computed using the LOTOS-EUROS model with true emissions, which are calculated according to the PH and MER given in Table 1. Fifty percent Gaussian noise is added to the data according to the uncertainty in the retrieval of satellite data as suggested by *Wen and Rose* [1994] and *Fu et al.* [2015]. The background emissions are computed with an overestimation of MER. This cautious approach is recommended in practice for advising commercial jet operations in airspace affected by volcanic ash. A correspondingly higher PH is used according to the empirical formula (11).

For the construction of $\mathbf{R}_k$ and $\mathbf{B}$ in the cost function (equation (A5)), 50% uncertainty is assumed in both observations and parameters with $\mathbf{R}_k$ and $\mathbf{B}$ in form of a diagonal matrix $\mathbf{R}_k^{-1} = (1/\sigma_k^o)^2\mathbf{I}^o$ and $\mathbf{B}^{-1} = (1/\sigma^b)^2\mathbf{I}^b$. To compare the influence of the assimilation window length on the estimates, assimilation windows of 1, 3, or 6 h are used. Using a larger assimilation window implies that more observations are incorporated. During one episode the eruptive parameters are assumed to be constant. All assimilation windows are shorter than the eruption episodes. In practice, an assimilation window of constant length should be used within one episode.

To generate the penalty term and the new background term as described in section 2.2, $f_m = 0.8$ is used in the penalty term. This value is based on experience. It means that 80% of the MER is assumed to be distributed at the injection layer. The injection layer is computed according to the PH information from the IMO observations. To make it more realistic, this MER is computed by applying formula (5) to the synthetic observations, not the MER of the "truth" in Table 1. To compare the two modifications, the new background term is calculated correspondingly with 80% of MER distributed at the injection layer and 20% of MER evenly distributed across other layers above the summit.

To test the impact of the estimate on the forecast, results with respect to the initial condition and the free forecast are computed. Data assimilation is iteratively applied with a 1 h assimilation window till the end of the first episode at 19:00 UTC, 14 April. The initial condition, which is the initial state field for the forecast run, is computed using the model with estimated emissions as reconstructed at the end of the assimilation. A forecast with the prior emission using this initial condition, denoted as "free forecast," is computed for the next period of 24 h. The result of the free forecast is given at 19:00 UTC, 15 April. The timeline is shown in Figure 3.

5.2. Estimates of Emission and Discussion

To test the impact of incorporating the additional information on the accuracy of the estimates, we use different assimilation windows and the two schemes of weighting the correction terms as mentioned in section 2.2. The results are shown in Figure 4, where estimated represents the solution obtained from cost function (A5) with only ash-column observations and the assumed background, est_pc represents the solution of cost function (4) with penalty term correction, est_bc represents the solution of cost function (7) with the background term correction, and bg_new represents the new background emission used in the background term correction.

First, we evaluate the impact of incorporating additional information. It can be observed that large oscillations occur in the estimated solution, and it may even be impossible to identify the injection height correctly (Figure 4a or 4d). This might be caused by the meteorological fields where some layers have similar meteorologic patterns, by the large uncertainty in observation data or by the nonlinearity in the volcanic ash model. The estimates with penalty term (est_pc) or new background term (est_bc) are significantly more accurate. Both ways of adding information work well in order to restrict the injection height (comparing estimated against est_pc or est_bc in Figure 4a or 4d). We can also notice that est_pc is closer to estimated at the layers other than the injection layer. Therefore, when estimated is reliable, penalty term correction is suggested to achieve a more accurate vertical profile than using background term correction. Note that the use of correction terms aims at capturing the injection layer. The maximum emission rates might be an

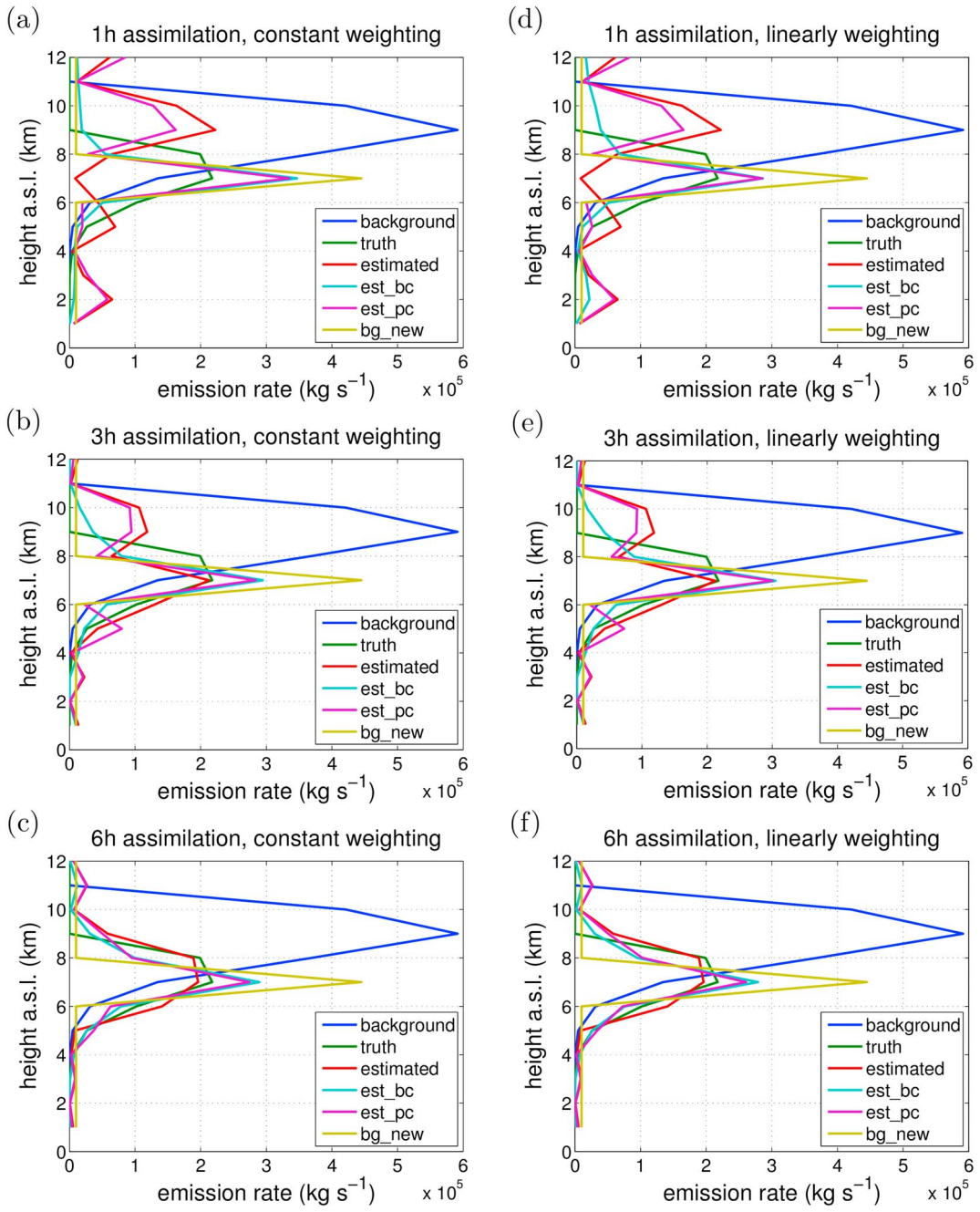

Figure 4. Estimation of the vertical profile of the volcanic ash emission at 19:00 UTC, 14 April 2010, using modified Trj4DVar. Computed with (a–c) constant weight factors (α_m and α_h) and with (d–f) weight factors as linear functions of the length of assimilation windows: using assimilation windows of 1 h in Figures 4a and 4d, 3 h in 4b and 4e, and 6 h in 4c and 4f.

underestimation or, in this case, an overestimation of the truth. Therefore, f_m in cost function (6) and the weight factors (α_h, α_m in equation (4) and α_b in equation (7)) should be adjusted to change the influence of the correction terms.

Second, we consider the influence of the length of assimilation window to the estimation results. By comparing estimated solutions in one column (for instance, Figures 4a–4c), it can be observed that when the assimilation window is enlarged, oscillations are decreased, and emissions are estimated more accurately. Especially the injection height and the basic shape of the profile are preserved in the 6 h situation. Moreover, the influence of the background (a priori information) on the estimates reduces with an increasing assimilation

window, since the estimates are improved and consequently the importance of the background is decreased (Figures 4a–4c).

Finally, the impact of the weights of the correction terms (α_h, α_m in equation (4) and α_b in equation (7)) is analyzed. By comparing the figures in one column, we observe that the influence of the additional information decreases with the length of assimilation window when constant weight factors are used (Figures 4a–4c), and the influence remains the same when the other set of weight factors is used (Figures 4d–4f). A constant weighting scheme is suggested when AML has a large uncertainty, since it makes the solution closer to the estimated solution when the assimilation window is enlarged and the accuracy of estimated is improved. Linear weight factors with small values are suggested when AML has a small uncertainty. Note that the weighting schemes are provided for assimilation windows with adjustable length. They are not considered when assimilation windows with constant length are used (section 6).

5.3. Forecasts of Ash Clouds

In this section, the predictive performance of the assimilation with or without the additional information of PH and MER will be analyzed.

As shown in the previous section, the original estimates and the estimates with correction terms differ more when using 1 h assimilation window than larger assimilation windows. Therefore, the forecasts using a 1 h assimilation window will be better for illustrative purpose. We apply data assimilation sequentially with a 1 h assimilation window during the first eruptive episode and simulate the model with the assimilation results until the end of the first episode (19:00 UTC, 14 April 2010). The ash columns after simulation, which can be regarded as the initial condition for the forecast run, are illustrated in Figures 5a–5d. It can be noticed that both estimated results (Figures 5c and 5d) are significantly improved with the mass loadings much closer to the forecast with the true emissions (Figure 5a).

Although the total column shows great resemblance, there are differences when looking into the details in each layer. This is because the wind fields change with the altitude, and the ash particles released at different layers transport differently. Therefore, each specific vertical profile of emissions will lead to a unique ash cloud which is distinguishable as shown in the initial conditions at the seventh layer over the vent in Figures 5e–5h. This implies that, in practice, although ash clouds generated with poorly estimated emissions often appear to match the satellite image (Figures 5e and 5 g), the interior 3-D ash concentrations may be far from the truth (Figures 5e and 5 g). However, with the incorporation of the additional information, both the ash mass loadings (comparing Figures 5a, 5b, and 5d) and the 3-D ash fields (comparing Figures 5e, 5f, and 5h) improve a lot. This implies that the correction terms are able to improve the initial condition with a more accurate estimate of the emissions, resulting in a more reliable forecast. This is confirmed by the results in Figure 5i–5l, which shows the free forecast until 10:00 UTC, 15 April 2010 simulated in the European domain with the same emissions and initial conditions as used for the model simulation in Figures 5a–5d. The pink box marks the area where ash emitted from the first episode was transported to. We can see that the shapes and positions of ash clouds vary (Figures 5k and 5l) with different initial fields (Figures 5g and 5h), and apparently a better estimation of the emission leads to a more reliable forecast which is closer to the truth (Figures 5i, 5k, and 5l).

6. Field Data Experiments

After having evaluated the method using synthetic data, now experiments with field data are conducted to explore the potentials of applying the method to realistic volcanic ash problems.

6.1. Experimental Setup and Preprocessing of the Data

In the field data experiments, the background (a priori) emissions are calculated according to the PH and MER given in Table 1. We use the hourly averaged mass loadings from the SEVIRI volcanic ash products to estimate the emission rates of the first eruptive phase of Eyjafjallajökull event. The validated data are available from 00:00 UTC, 14 April 2010 to 23:45 UTC, 22 May 2010. The data of 12:00–18:00 UTC, 15 April, are used to carry out the assimilation, and future data are used to validate the results of the forecasts. The 6-hourly averaged PH and MER information shown in Figure 2b is integrated in the assimilation process through the penalty correction and background correction methods. A 6 h assimilation window is used since this has been shown as the best settings in section 5. We only use tracers of vash_4 – vash_6 in Table 2, because large particle will fall out of the ash plume very soon and will have little contribution to the forecasts. Furthermore, the SEVIRI instrument is sensitive to small particles with radii 1μm–16μm [*Prata and Prata*, 2012]. Subsequently, the value

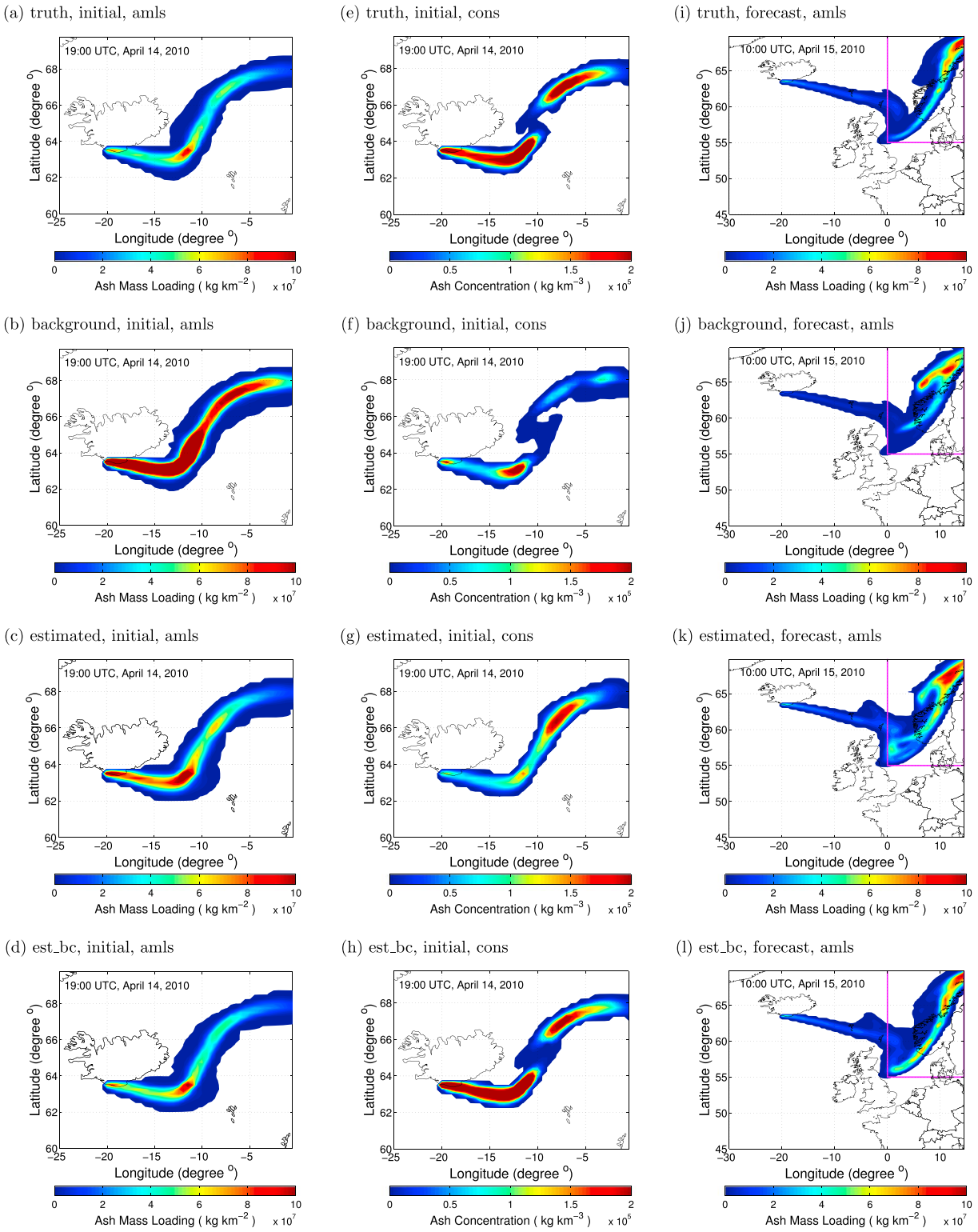

Figure 5. Comparison of the simulation results with assimilation and without assimilation. Figures in different rows represent results simulated with different emissions of: (a, e, and i) the truth, (b, f, and j) the background, (c, g, and k) the estimate with assimilation of PH and MER, and (d, h, and l) the estimate without assimilation of PH and MER. Figures 5a–5d are the AMLs of the initial conditions at 19:00 UTC, 14 April 2010. Figures 5e–5h are the ash clouds at the seventh layer over the vent of the initial condition, at 19:00 UTC, 14 April 2010. Figures 5i–5l are the AMLs of the free forecast at 10:00 UTC, 15 April 2010, initiated from 19:00 UTC, 14 April 2010.

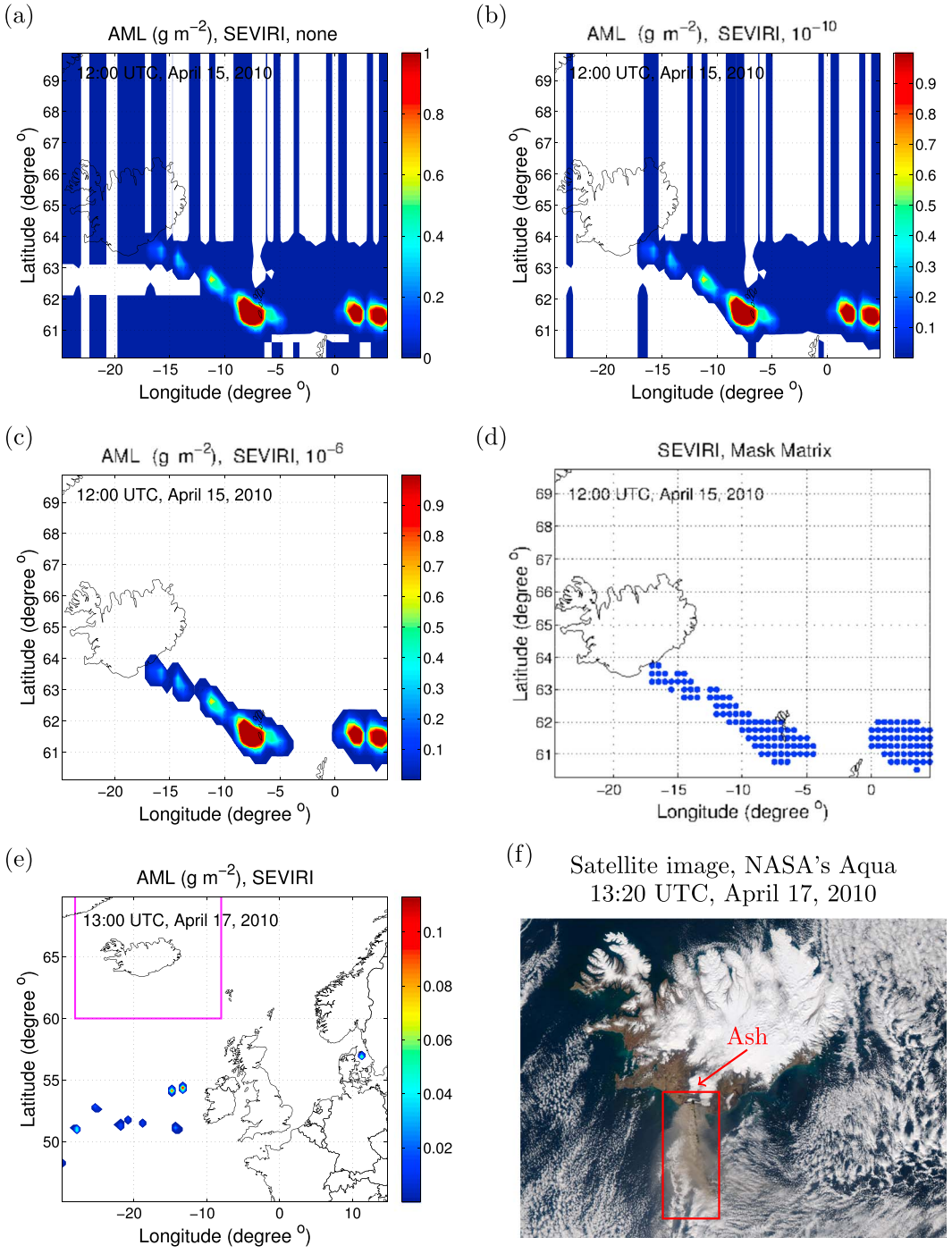

Figure 6. Preprocessing of SEVIRI data to remove retrieval noise with thresholds and eliminate the influence of an invalid detection of ash with a mask matrix. (a–c) The illustrations of the retrieval noise (dark blue "bands") and SEVIRI AMLs (g m^{-2}) filtered with different thresholds: no threshold (Figure 6a), thr = 10^{-10} (Figure 6b), and thr = 10^{-6} (Figure 6c). (d) The illustration of mask matrix corresponding to Figure 6c. (e–f) The illustrations of invalid detection with: AML of SEVIRI data showing no ash detected in the pink box (Figure 6e) and image obtained by ASA's MODIS satellite showing a clear ash plume in the red box (Figure 6f).

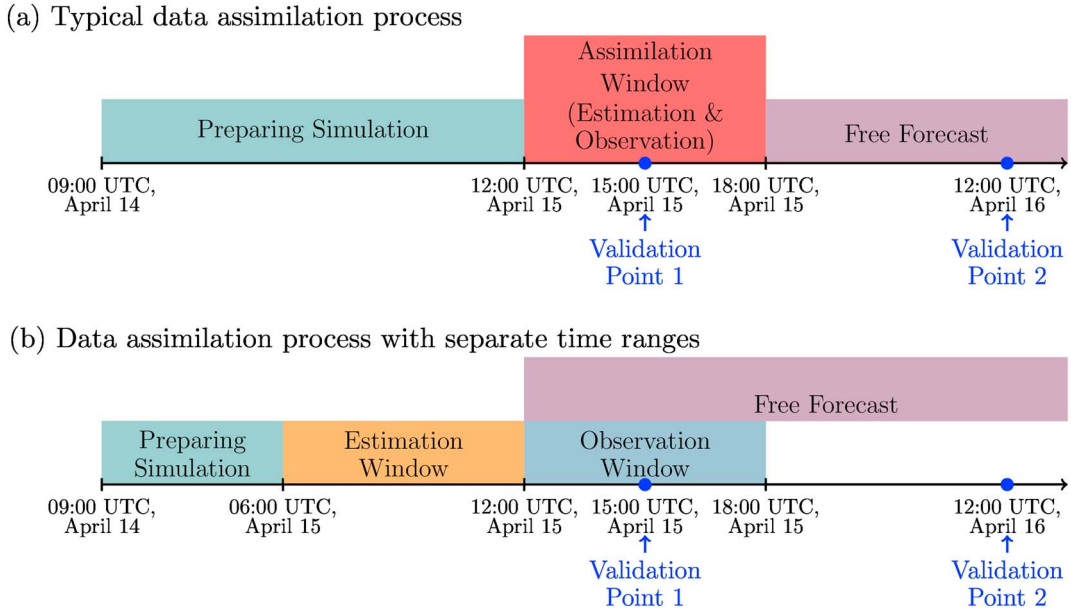

Figure 7. Timelines of real data experiment for (a) typical assimilation process and (b) assimilation process with separate time ranges.

of MER to be assimilated is scaled with the SCAF accordingly. The SCAF value is a percentage of the total MER including particles ranged from vash_4 to vash_6.

To properly use the SEVIRI AML data, a threshold valued 10^{-6} (g m^{-2}) is adopted to screen out the invalid data below this threshold. The values below this threshold are set to zero in this study. Alternatively, they can be set to NaN or negative values. Noise is the result of the observational uncertainty of the instrument and the errors introduced by the retrieval algorithm. Figure 6a illustrates the noisy AML field of the original SEVIRI data, where the "dark blue bands" indicate the noise resulted from the retrieval algorithm with the values above zero. Figure 6c shows the clean AML field used in the experiment. The threshold is manually tuned and selected based on experimental results, which is able to filter out the dark blue bands while preserve most of the usable data.

Besides noise, invalid data can also be the result of undetectable ash or incorrectly detected ash. Figures 6e and 6f demonstrate a case of invalid ash detection. In the boxed area of Figure 6e there appears to be no ash detection from the SEVIRI data with zero values. However, NASA's Moderate Resolution Imaging Spectroradiometer (MODIS) satellite gives a clear observation of volcanic ash in the corresponding area (Figure 6f). In this case, assimilating the data of the entire domain or in the boxed area in Figure 6e will result in inaccurate estimates.

The original zero values (without being processed by the threshold) imply no ash detected, but it is difficult to determine whether that corresponds to really no ash in the real world. The use of the original zero to constrain the pixels without plume could be misleading and could influence the estimates negatively. Therefore, we only use the pixels where ash is clearly detected. To eliminate the disturbance of invalid data to the estimates, after the threshold is employed, we generate a mask matrix to select/mark the valid data area (pixels with values above zero). If the pixels containing original zeros are further confirmed and validated with extra knowledge to be no ash affected, these pixels can be marked so that the zeros will constrain where the plume should not be. An illustration of the mask matrix generated from Figure 6c is given in Figure 6d with selected pixels shown by blue dots. Consequently, the target of DA is to obtain the estimate of emission which will lead to an ash cloud matching the SEVIRI AML data the most in the selected area by the assimilation of preprocessed data above zeros.

6.2. Results With Different Estimation Windows

In a typical assimilation process, the time range of the parameters to be calibrated (estimation window) coincide with that of the observations to be assimilated (observation window), represented by the assimilation

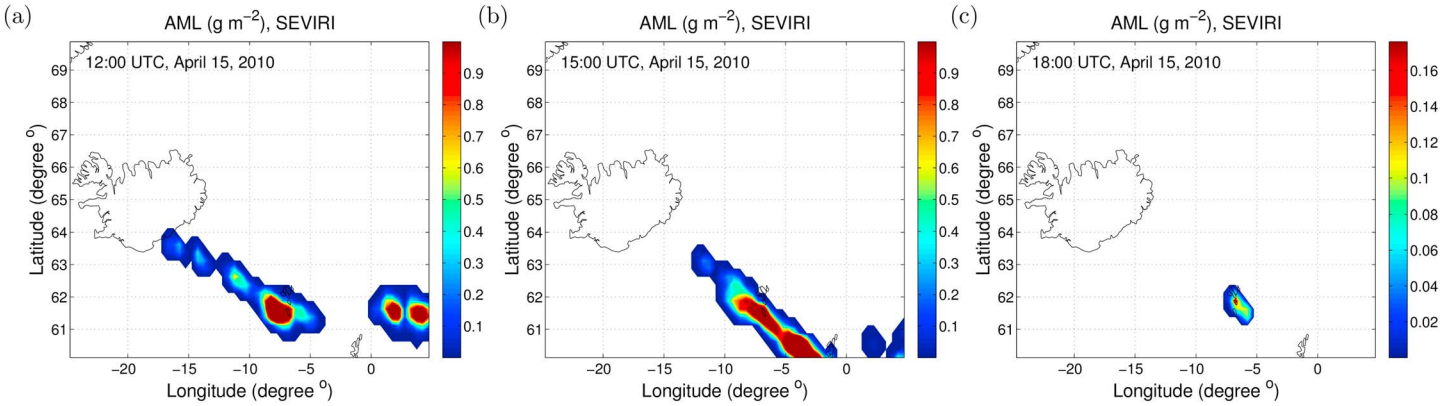

Figure 8. AMLs of SEVIRI during the observation window 12:00–18:00 UTC, 15 April 2010, chosen at time: (a) 12:00 UTC, (b) 15:00 UTC, and (c) 18:00 UTC.

window in Figure 7a. In this section, we use an estimation window separately from the observation window as shown in Figure 7b and test the performance of using different estimation windows.

We assimilate the observations during 12:00–18:00 UTC, 15 April 2010. Figure 8 gives a series of AML fields of SEVIRI to be assimilated. Notice that there is no valid data near the summit (<250 km from Iceland) in Figures 8b and 8c where newly emitted ash (<3 h) should be transported to. Since the detected ash clouds (colored pixels) consist of emissions earlier than 12:00 UTC, 15 April 2010, it is not appropriate to estimate emissions after 12:00 UTC using this data. Therefore, we choose an estimation window by roughly tracing back the emission time from the valid data areas in the observation window according to the wind speeds. Note that the estimation window and observation window can overlap or can be totally different due to specific meteorological conditions.

The estimation results of applying both assimilation processes are given in Figure 9. Here the estimate is denoted as "earlier estimate" when using separate time ranges (with an earlier estimation window) and denoted as "normal estimate" when using a typical assimilation time range. It is shown that both correction methods (est_bc and est_pc) will restrict the maximum of the emission rate at the injection height, 5.5 km in this case. This confirms the conclusion from the twin experiments.

We explore the impact of using different estimation time ranges with respect to estimating the initial condition. Usually, the initial condition is available when the free forecast starts, i.e., at the end of the estimation window. However, in this case, the two assimilation processes have different initial times for the free forecasts. For the purpose of comparison, we use a shared initial time at validation point 1 (15:00 UTC, 15 April). This point is chosen because it should be later than 12:00 UTC so that the estimated emissions of both

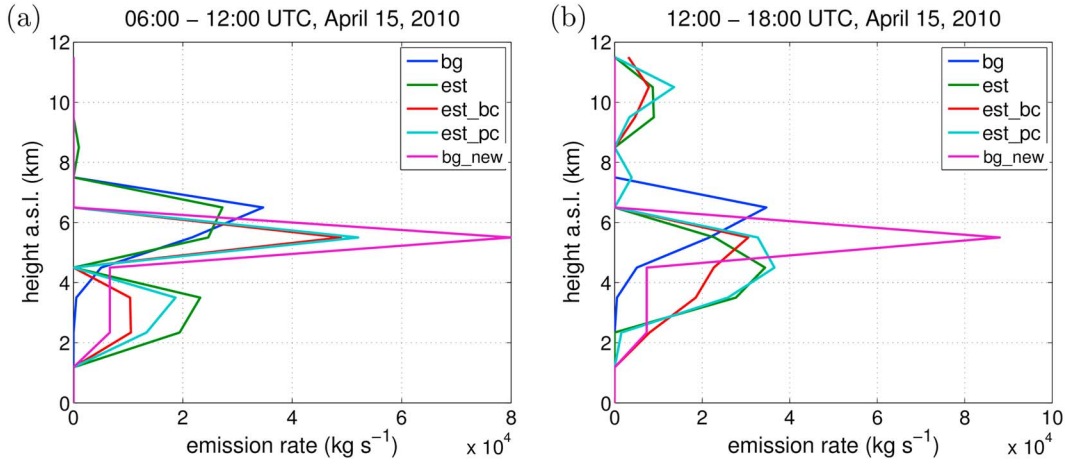

Figure 9. Estimation results of emissions during the estimation window of (a) 06:00–12:00 UTC and (b) 12:00–18:00 UTC, 15 April 2010.

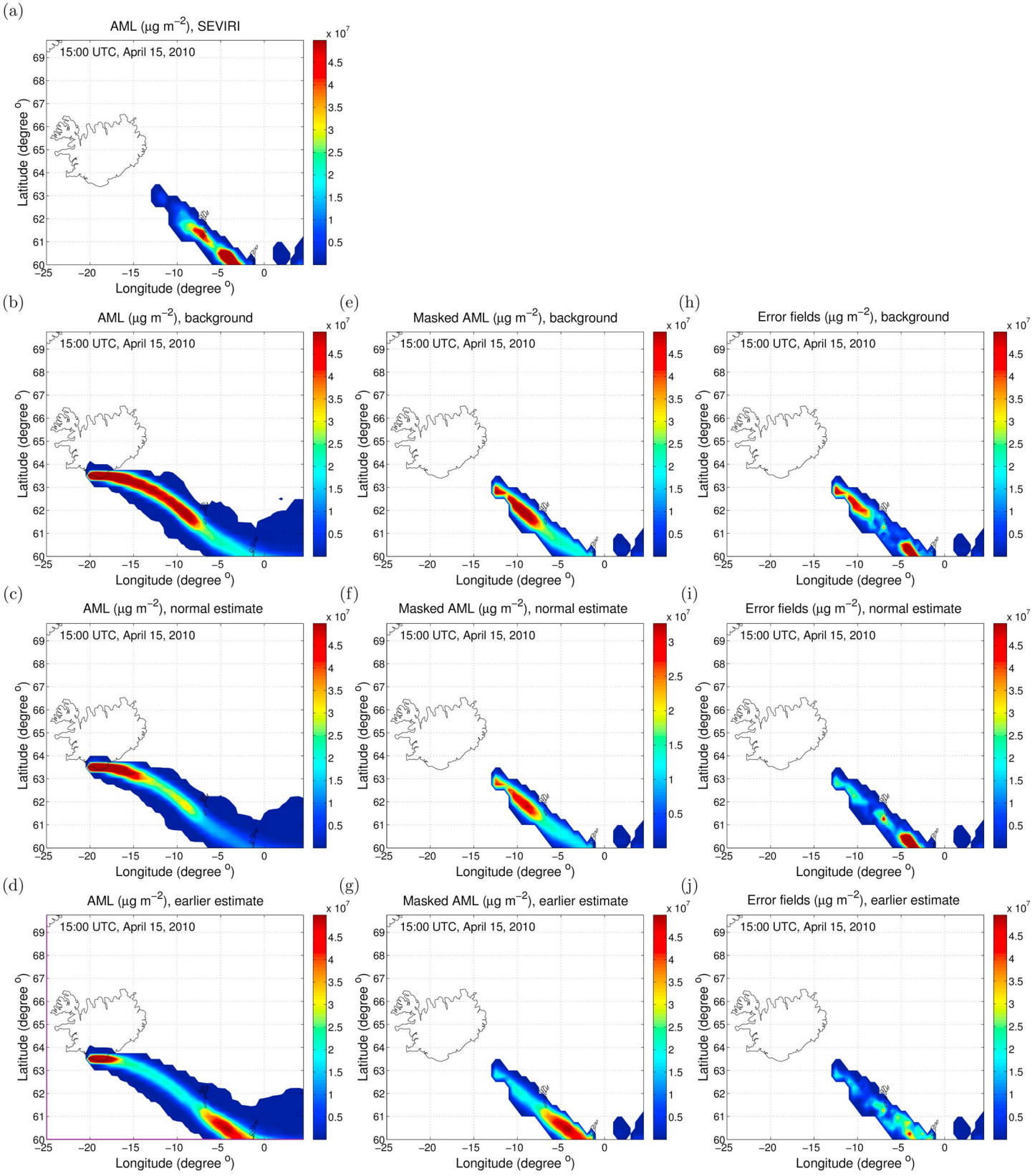

Figure 10. Initial conditions (AML) at 15:00 UTC, 15 April 2010, simulated with (b) background emission, (c) normal estimate, and (d) earlier estimate. (e–g) The AML fields of Figures 10b–10d in the masked area. (h–j) The error fields of Figures 10e–10g compared to (a) the SEVIRI AML fields.

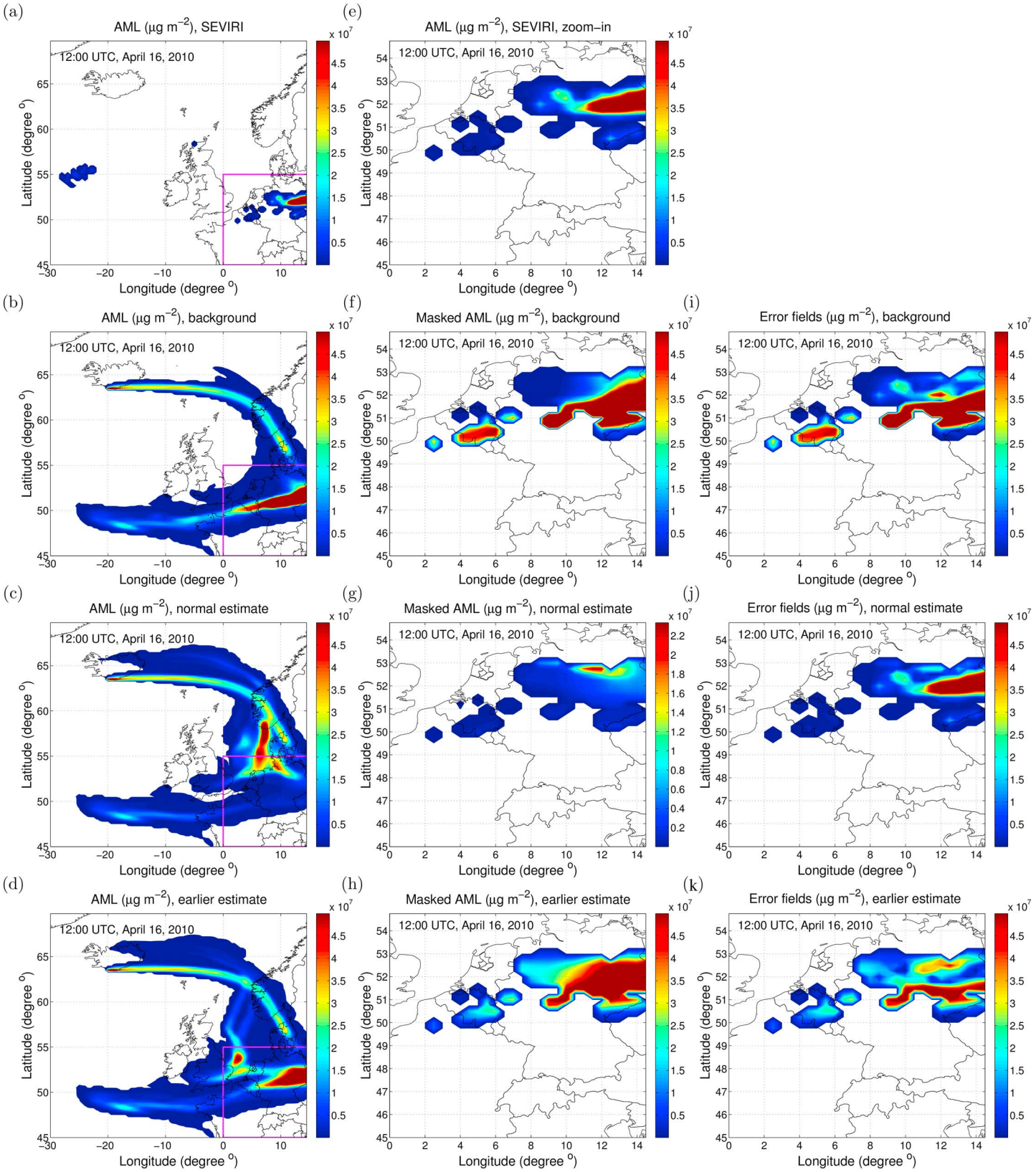

Figure 11. Free forecasts (AML) at 12:00 UTC, 16 April 2010, simulated with (b) background emission, (c) normal estimate, and (d) earlier estimate. (f–h) The zoomed-in AML fields of Figures 11b–11d in the masked area. (i–k) The error fields of Figures 11f–11h compared to (a and e) the SEVIRI AML fields.

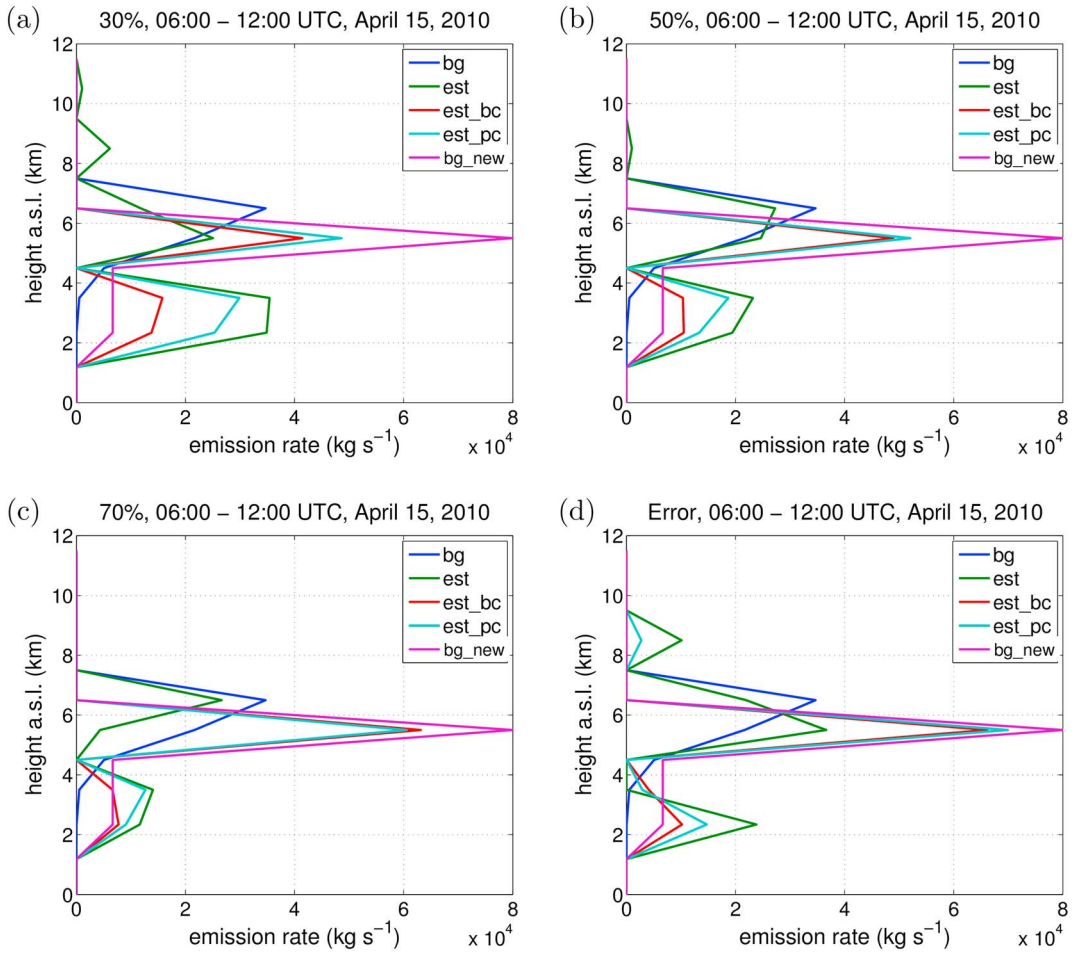

Figure 12. Estimation results of emission during 06:00–12:00 UTC, 15 April 2010, with observational error covariance matrices generated with assumption of (a) 30% uncertainty, (b) 50% uncertainty, (c) 70% uncertainty, and (d) the SEVIRI retrieval error data.

assimilation processes can influence the initial condition, and the masked area of SEVIRI should be large enough to clearly observe the influences.

The initial conditions are shown in Figure 10. By comparing Figures 10b–10d, we can see that both assimilations have influence on the initial condition. However, the earlier estimate affects the whole masked area, while the normal estimate affects the tip in the northwest of the masked area, since with the normal estimate ash cannot be transported that far in such a short period (compare the masked area in Figures 10e–10g and compare the error fields in Figures 10h–10j). This implies that the ash clouds in the masked areas of 12:00–18:00 UTC come mostly from the emission during 06:00–12:00 UTC.

The free forecasts till 12:00 UTC, 16 April (validation point 2), are shown in Figure 11. It should be noticed that in (Figures 11b–11d), forecasts show a large plume throughout the European domain, but SEVIRI data show no ash detected around Iceland (Figure 11a). It is difficult to determine which is correct since the free forecast is formed with the a priori emissions which have a large uncertainty; meanwhile, no ash detected does not necessarily imply no ash presenting as illustrated Figures 6e and 6f. Therefore, we use the masked area for validation and use the whole domain for a general comparison. It can be seen in the left column that the ash of earlier estimate has been transported to the masked area in the pink box, while the ash of normal estimate has only been transported there partly. Moreover, by observing the middle column and the right column, we can see that the earlier estimate corrects the whole masked area, while the normal estimate hardly has influence in that area. This further confirms the conclusion that using the earlier estimation window is more proper in this case.

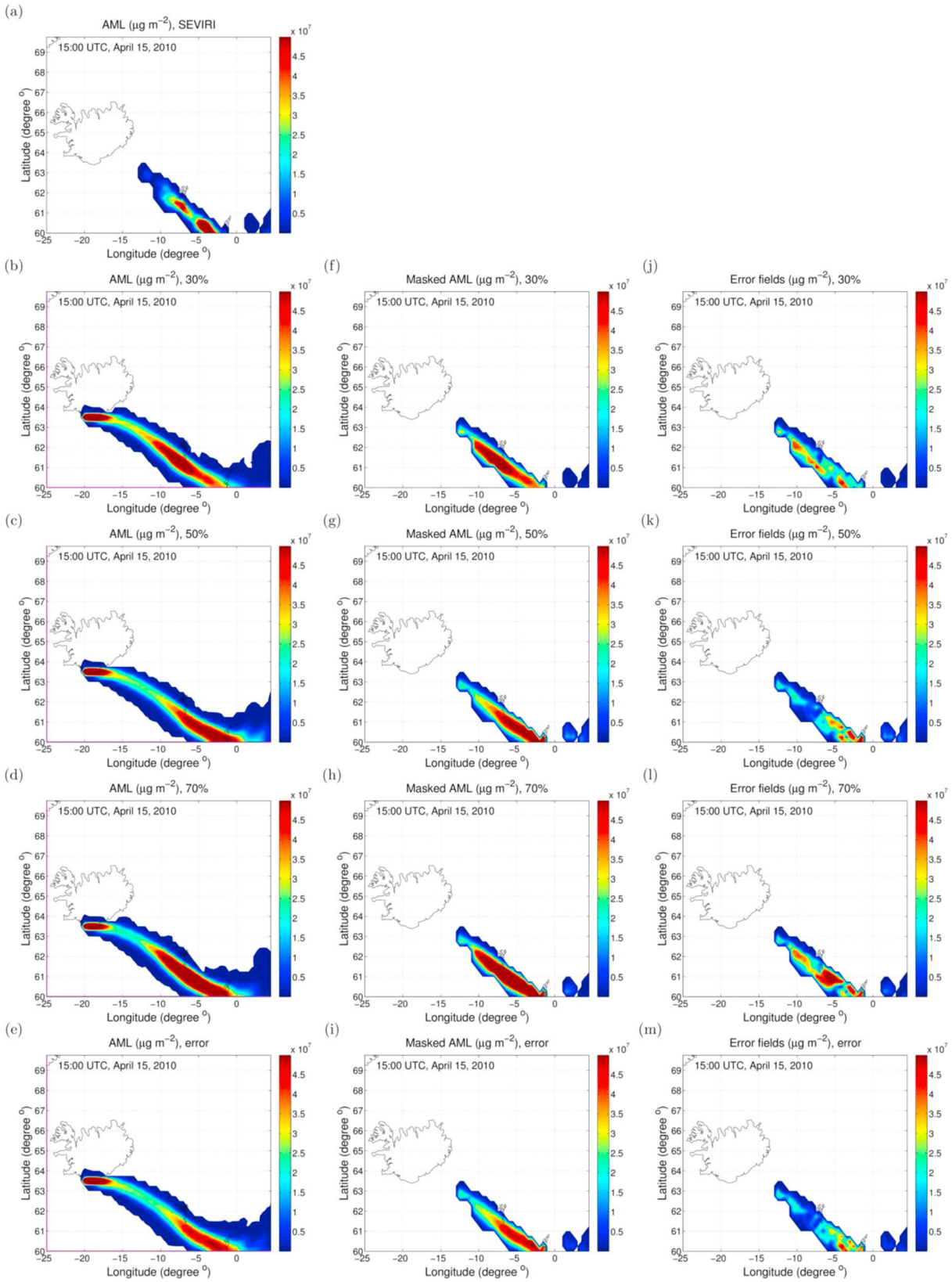

Figure 13. Initial conditions (AML) at 15:00 UTC, 15 April 2010, simulated with estimates of the observational error covariance matrices generated with assumption of (b) 30% uncertainty, (c) 50% uncertainty, (d) 70% uncertainty, and (e) the SEVIRI retrieval error data. (f–i) The AML fields of Figures 13b–13e in the masked area. (j–m) The error fields of Figures 13f–13i compared to (a) the SEVIRI AML fields.

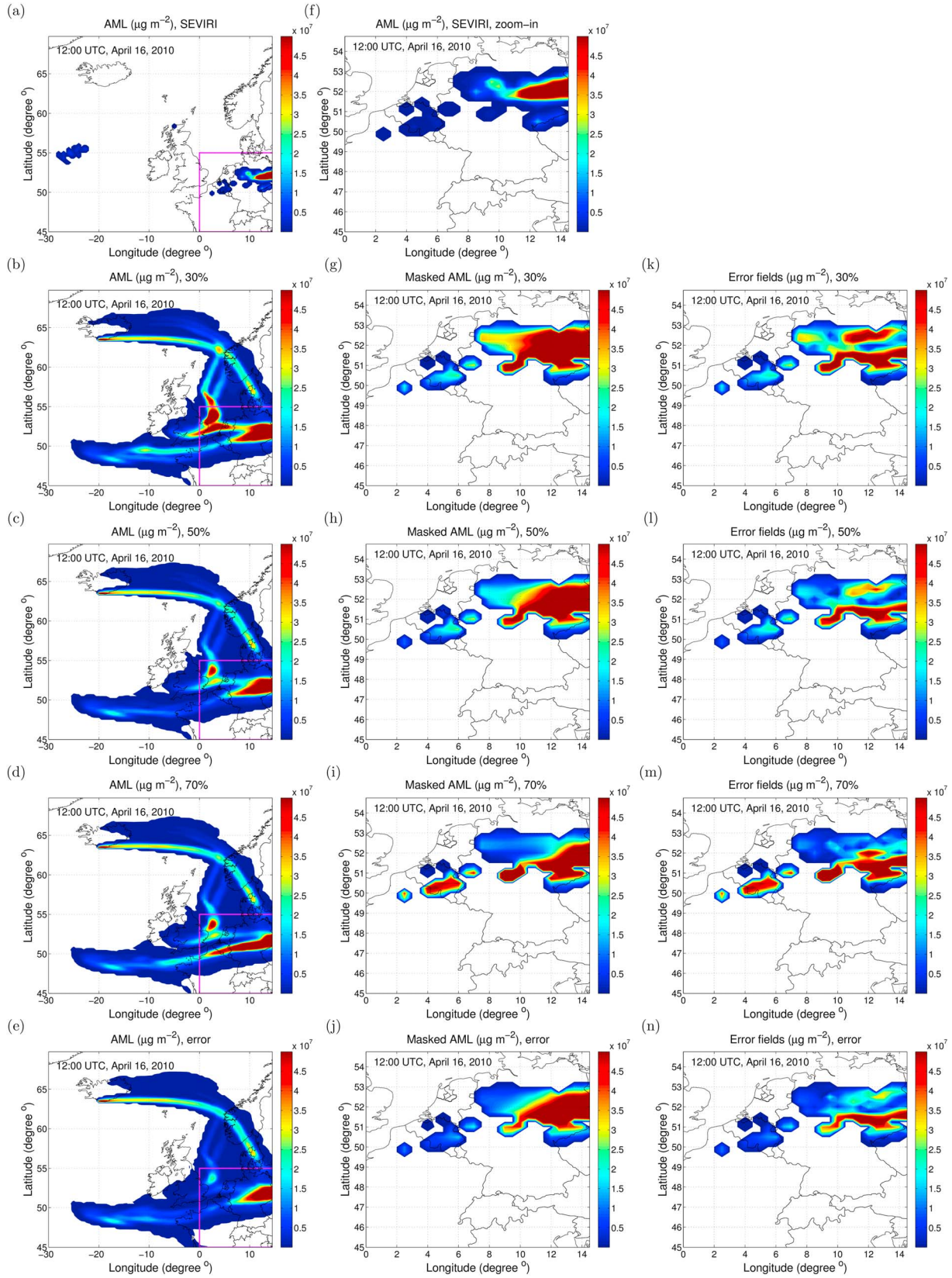

Figure 14. Free forecasts (AML) at 12:00 UTC, 16 April 2010, simulated with estimates of observational error covariance matrices generated with: (b) 30% uncertainty, (c) 50% uncertainty, (d) 70% uncertainty, and (e) the SEVIRI retrieval error data. (g–j) The zoomed-in AML fields of Figures 14b–14e in the masked area. (k–m) The error fields of Figures 14g–14i compared to (a and f) the SEVIRI AML fields.

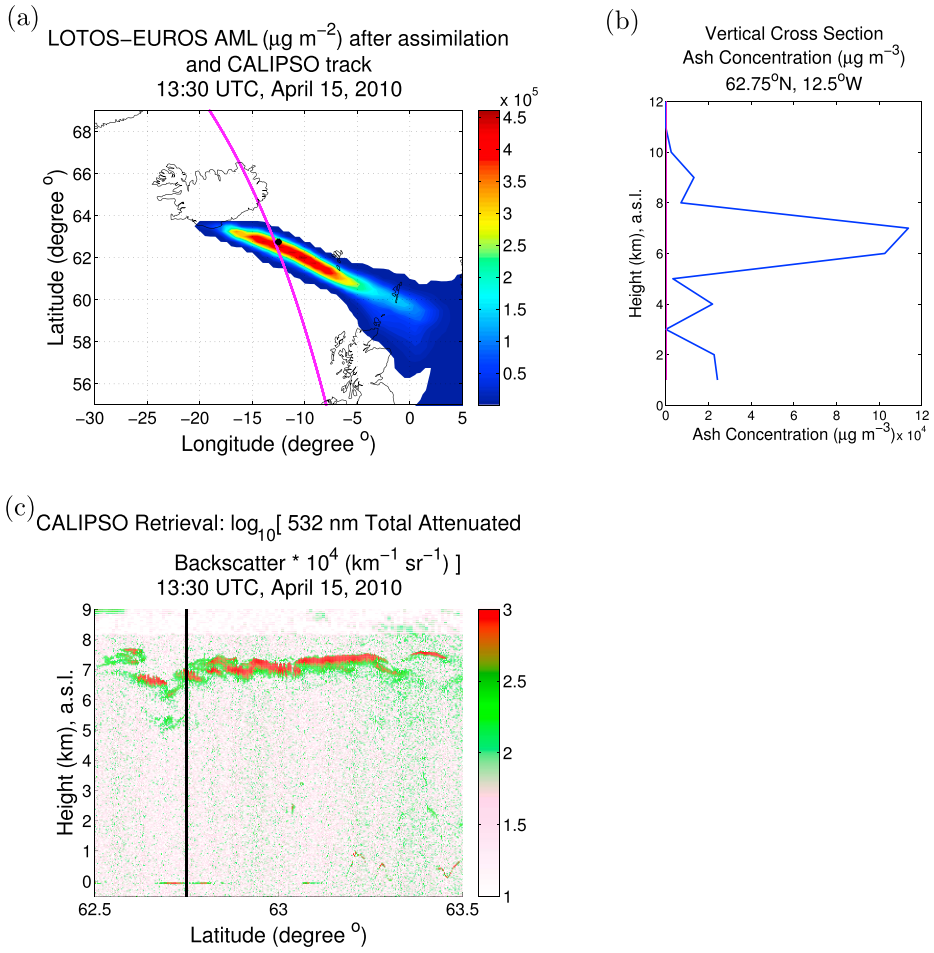

Figure 15. Comparison between the simulation results after the assimilation with the CALIPSO observations at 13:30 UTC, 15 April 2010: (a) LOTOS-EUROS-simulated volcanic ash forecast (AML), the CALIPSO track illustrated by the magenta curve, and the evaluation spot marked by the black dot; (b) vertical profile of volcanic ash concentration located at 62.75°N, 12.5°W, marked by a black dot in Figure 15a, and (c) CALIPSO total backscatter at 532 nm.

6.3. Results With Different Observational Error Covariance Matrices

In this section, we compare the influence of different observation error covariance matrices in the field data case. We use the earlier estimation window of 06:00–12:00 UTC in Figure 7b and diagonal error covariance matrices generated with 30%, 50%, 70% uncertainty, and the SEVIRI retrieval error data. Note that theoretically, retrieval error data with high quality will provide a better latent information on the observational uncertainties than the Gaussian-distributed assumptions.

The estimation results are shown by Figure 12. By observing the original estimation results without using correction schemes, i.e., est shown by the green lines, it can be noticed that 30% uncertainty is an underestimation so that the injection height is not well identified, since the lower spike is larger than the spike at the injection layer; 70% uncertainty is an overestimation so that the estimate is too close to the background emission and observation data have little effect on the DA process. The 50% uncertainty balances the influence of the background emission and the observations. In addition, by observing the length of spike at the injection layer of the estimation with the penalty correction (est_pc) or background correction (est_bc), the correction algorithm has an increasingly correcting effect with higher observational uncertainty.

The initial conditions displayed in Figure 13 are computed from the original estimated emissions, i.e., est solutions in Figure 12. We are testing the influence of observational uncertainties on the forecasts, so we choose among est, est_pc, and est_bc for the one that can be distinguished the most by the use of a different uncertainty. In Figure 13, although the entire ash clouds look similar in the Figures 13b–13e, it can be noticed

from Figures 13f–13i that the clouds vary in the masked area. Figures 13j–13m give the error fields using data assimilation. Here we observe that using 50% uncertainty or retrieval error data results in a more accurate initial condition.

The free forecasts are shown in Figure 14. We can see that the shapes and positions of the red parts formed by the estimated emissions in Figures 14b–14e vary. From Figures 14g–14j, it can be seen that 70% uncertainty (Figure 14i) works the worst on the assimilation since the red parts cover a larger area (the Belgium area) compared to the SEVIRI Figure 14f, while uncertainties of 50% and 30% work similarly as shown in Figures 14h and 14g. However, Figure 14c seems to be more reasonable with smaller concentrations than 14b around the Netherlands, Belgium, Luxembourg, and northern France. Using error data produces a forecast (Figure 14j) which matches the best to the red parts in the SEVIRI figure (Figure 14f). Figures 14k–14n confirm what we observe from Figures 14g–14j, using 30% uncertainty has little influence in the masked area, while using 50% and 70% uncertainties can correct the ash-dense area (red parts) partly. Using the retrieval error data corrects most of the ash-dense area.

6.4. Evaluation With CALIPSO Data

Additional spaceborne data are available from the Cloud-Aerosol Lidar with Orthogonal Polarization lidar on the Cloud-Aerosol Lidar and Infrared Pathfider Satellite Observation (CALIPSO) platform [*Winker et al.*, 2012]. These data are used for the evaluation of the vertical structure of the simulated ash cloud after the assimilation. We analyze the total attenuated backscatter signal at 532 nm, which responds to aerosols including volcanic ash. On 15 April at 13:30 UTC, CALIPSO passed over the ash cloud (Figure 15a) and detected the cloud at around 6–7 km above sea level (asl) from 62.5°N to 63.5°N (Figure 15c).

The simulated AML results after the assimilation is shown in Figure 15a. We can see that the position where ash cloud with high concentration passes the CALIPSO track (62.5°N–63.5°N) is in agreement with the CALIPSO data. We also evaluate the vertical ash concentration profile at 62.75°N, 12.5°W using the CALIPSO data near this location. The altitude (around 6–7 km) and thickness (around 1 km) of the simulated ash cloud (Figure 15b) are clearly similar to the observations (Figure 15c).

7. Conclusion and Discussion

In this paper, we have explored the potentials of applying the trajectory-based 4D-Var (Trj4Dvar) approach to estimate the volcanic ash emissions using ash mass loadings retrieved from SEVIRI data. In a previous study [*Lu et al.*, 2016], we found that a standard 4D-Var approach is incapable of estimating the vertical profile of volcanic ash emissions or of determining the injection height using satellite ash column data. Therefore, Trj4DVar was proposed, and results of twin experiment conducted on a simplified model showed that the approach perform well with large assimilation windows and with synthetic observations of ash columns.

In this paper, we tested Trj4Dvar on a 3-D realistic (full) model (LOTOS-EUROS) using both synthetic observations and real satellite data. We found that using a small assimilation window (1 h or 3 h) generates unstable solutions. However, when using 6 h assimilation windows, the injection height was not always accurately determined, especially when using real satellite data. Therefore, we propose a modification of Trj4DVar to include additional information of the plume height and the mass eruption rate. The modified approach was tested with twin experiments. The results show that the injection layer could be captured well, and more accurate initial conditions were achieved. The forecast of ash cloud was also improved.

The modified Trj4DVar approach was also tested with real satellite data—AML retrieved from SEVIRI observations. We have discussed what the preprocessing of the data was and proposed a procedure to exclude the influence of retrieval noise and the invalid detection of ash on the assimilation results. This preprocessing is necessary for achieving a more accurate estimate of the emissions. It is not a time-consuming procedure where the computational cost for data to be assimilated is much less than one model simulation during the assimilation window.

Due to the insufficiency of the data, it was suggested to estimate the emission using a proper time range which does not necessarily coincide with the observational time range. The emission time range was computed by tracing back to where the ash released covered most of the valid data area. Furthermore, we suggest to use the retrieval error data, which were obtained as a by-product of the ash mass loading data, in the construction of observational error covariance matrix as an extra benefit from the satellite data.

The modified Trj4Dvar showed good performance on this case study. Its computational cost was affordable (33 min using 6 h assimilation window on a computer mentioned in section 4, or about 13 forward simulations in our case). Therefore, the modified Trj4Dvar bears a great potential for use in operational volcanic ash forecasting using assimilation of ash columns in conjunction with ground-based observations of PH and MER. In other applications, the information of PH and MER may not be averaged and validated every 6 h; thus, assimilation windows of adaptable length could be considered. In order to utilize data of other satellite instruments, adjustments should be made in the preprocessing of the data and in the specification of the observational uncertainty. For instance, the construction of the observational error covariance can be adjusted according to the retrieval error data.

Appendix A: Trajectory-Based 4D-Var

Trj4DVar seeks an optimal linear combination of trajectories generated with different emissions to fit the observation data coupled with a priori information, by minimizing a reformulated 4D-Var cost function.

In order to estimate the (average) emissions over an assimilation window $[t_0, t_N]$, the emissions are assumed to be constant and denoted by $\boldsymbol{u}$. The vector $\boldsymbol{u}$ is in a parameter space spanned by the perturbed parameter sets $\Delta\boldsymbol{u}^i$ $(i=1,\cdots,p)$ in the following form:

$$\boldsymbol{u} = \boldsymbol{u}^b + \sum_{i=1}^{p} \beta^i \Delta\boldsymbol{u}^i, \tag{A1}$$

where $\boldsymbol{u}^b$ is the background or first guess of emission rate, $\Delta\boldsymbol{u}^i$ is a perturbation of the emission rate in the ith layer over the vent, and β^i is the weight of $\Delta\boldsymbol{u}^i$ in the sum. Therefore, the determination of $\boldsymbol{u}$ corresponds to the estimating $\boldsymbol{\beta} = \left[\beta^1, \cdots, \beta^p\right]$.

First, trajectories are computed with a reference simulation using the background input:

$$\boldsymbol{y}_k^0 = \mathcal{H}_k\left(\mathcal{M}_k\left(\boldsymbol{x}_{k-1}, \boldsymbol{u}^b\right)\right). \tag{A2}$$

Second, and a set of associated simulations with perturbed parameters is computed:

$$\Delta\boldsymbol{y}_k^i = \mathcal{H}_k\left(\mathcal{M}_k\left(\boldsymbol{x}_{k-1}, \boldsymbol{u}^b + \Delta\boldsymbol{u}^i\right)\right)\boldsymbol{y}_k^0. \tag{A3}$$

The observations in equation (2) can be approximated by the following:

$$\begin{aligned}
\boldsymbol{y}_k &\approx \mathcal{H}_k\left(\mathcal{M}_k\left(\boldsymbol{x}_{k-1}, \boldsymbol{u}^b\right)\right) + \sum_{i=1}^{p} \beta^i \boldsymbol{H}_k^{\mathrm{TL}} \boldsymbol{M}_k^{\mathrm{TL}}\left(\boldsymbol{x}_{k-1}, \Delta\boldsymbol{u}^i\right) + \boldsymbol{\gamma}_k \\
&\approx \boldsymbol{y}_k^0 + \sum_{i=1}^{p} \beta^i \left(\mathcal{H}_k\left(\mathcal{M}_k\left(\boldsymbol{x}_{k-1}, \boldsymbol{u}^b + \Delta\boldsymbol{u}^i\right)\right) - \boldsymbol{y}_k^0\right) + \boldsymbol{\gamma}_k \\
&= \boldsymbol{y}_k^0 + \sum_{i=1}^{p} \beta^i \Delta\boldsymbol{y}_k^i + \boldsymbol{\gamma}_k,
\end{aligned} \tag{A4}$$

where $\boldsymbol{H}_k^{\mathrm{TL}}$ and $\boldsymbol{M}_k^{\mathrm{TL}}$ denote the tangent linear model of $\mathcal{H}_k$ and $\mathcal{M}_k$, respectively. Therefore, the coefficients $\boldsymbol{\beta}$ can be computed by minimizing the cost function given by the following:

$$\begin{aligned}
J(\boldsymbol{\beta}) &= \frac{1}{2} \sum_{k=1}^{Nt} \left(\sum_{i=1}^{p} \beta^i \Delta\boldsymbol{y}_k^i + \boldsymbol{y}_k^0 - \boldsymbol{y}_k\right)^T \left[\mathbf{R}_k\right]^{-1} \left(\sum_{i=1}^{p} \beta^i \Delta\boldsymbol{y}_k^i + \boldsymbol{y}_k^0 - \boldsymbol{y}_k\right) \\
&\quad + \frac{1}{2}\left(\boldsymbol{u} - \boldsymbol{u}^b\right)^T \left[\mathbf{B}_k\right]^{-1} \left(\boldsymbol{u} - \boldsymbol{u}^b\right) \\
&= J^o + J^b,
\end{aligned} \tag{A5}$$

where J^o and J^b represent the observation term and the background term, respectively. When the number of parameters to be estimated is small (less than 100), which is the case in our application ($p < 100$), we can transform the optimization problem into an algebraic problem by demanding the gradient $\nabla J_{\boldsymbol{u}} = 0$ and solve it directly.

Acknowledgments
We thank Prata (Nicarnica Aviation AS, Gunnar Randers vei 24, NO-2007 Kjeller, Norway) for providing SEVIRI data and his suggestions on the use of the data. The data used in this study are available from the European Space Agency (ESA) project—Volcanic Ash Strategic initiative Team (VAST) and can be downloaded from http://vast.nilu.no/test-database/volcano/Eyjafjallajokull/eruption/2010-04-14/main_data_type/Satellite/specific_data_type/seviri/. (Registration required). We are very grateful to the Editor and reviewers for their reviews and insightful comments and suggestions. The first and the last author thank China Scholarship Council for the financial support.

References

Ansmann, A., et al. (2010), The 16 April 2010 major volcanic ash plume over central Europe: EARLINET lidar and AERONET photometer observations at Leipzig and Munich, Germany, *Geophys. Res. Lett.*, *37*, L13810, doi:10.1029/2010GL043809.

Arason, P., G. N. Petersen, and H. Bjornsson (2011), Observations of the altitude of the volcanic plume during the eruption of Eyjafjallajökull, April–May 2010, *Earth Syst. Sci. Data*, *3*(1), 9–17, doi:10.5194/essd-3-9-2011.

Bonadonna, C., and A. Costa (2013), Plume height, volume, and classification of explosive volcanic eruptions based on the Weibull function, *Bull. Volcanol.*, *75*(8), 1–19, doi:10.1007/s00445-013-0742-1.

Casadevall, T. J. (1994), Alaska Volcano Observatory—The 1989–1990 eruption of Redoubt Volcano, Alaska: Impacts on aircraft operations, *J. Volcanol. Geotherm. Res.*, *62*, 301–316.

Curier, R. L., R. Timmermans, S. Calabretta-Jongen, H. Eskes, A. Segers, D. Swart, and M. Schaap (2012), Improving ozone forecasts over Europe by synergistic use of the LOTOS-EUROS chemical transport model and in-situ measurements, *Atmos. Environ.*, *60*, 217–226, doi:10.1016/j.atmosenv.2012.06.017.

Dacre, H. F., et al. (2011), Evaluating the structure and magnitude of the ash plume during the initial phase of the 2010 Eyjafjallajökull eruption using lidar observations and NAME simulations, *J. Geophys. Res.*, *116*, D00U03, doi:10.1029/2011JD015608.

Dacre, H. F., A. L. M. Grant, and B. T. Johnson (2013), Aircraft observations and model simulations of concentration and particle size distribution in the Eyjafjallajökull volcanic ash cloud, *Atmos. Chem. Phys.*, *13*(3), 1277–1291, doi:10.5194/acp-13-1277-2013.

Eckhardt, S., A. J. Prata, P. Seibert, K. Stebel, and A. Stohl (2008), Estimation of the vertical profile of sulfur dioxide injection into the atmosphere by a volcanic eruption using satellite column measurements and inverse transport modeling, *Atmos. Chem. Phys.*, *8*(14), 3881–3897, doi:10.5194/acp-8-3881-2008.

Evensen, G. (1994), Sequential data assimilation with a nonlinear quasi-geostrophic model using Monte Carlo methods to forecast error statistics, *J. Geophys. Res.*, *99*(C5), 10,143–10,162.

Flemming, J., and A. Inness (2013), Volcanic sulfur dioxide plume forecasts based on UV satellite retrievals for the 2011 Grímsvötn and the 2010 Eyjafjallajökull eruption, *J. Geophys. Res. Atmos.*, *118*, 10,172–10,189, doi:10.1002/jgrd.50753.

Flentje, H., H. Claude, T. Elste, S. Gilge, U. Köhler, C. Plass-Dülmer, W. Steinbrecht, W. Thomas, A. Werner, and W. Fricke (2010), The Eyjafjallajökull eruption in April 2010—Detection of volcanic plume using in-situ measurements, ozone sondes and lidar-ceilometer profiles, *Atmos. Chem. Phys.*, *10*, 20, doi:10.5194/acp-10-10085-2010.

Fu, G., H. X. Lin, A. W. Heemink, A. J. Segers, S. Lu, and T. Palsson (2015), Assimilating aircraft-based measurements to improve forecast accuracy of volcanic ash transport, *Atmos. Environ.*, *115*, 170–184, doi:10.1016/j.atmosenv.2015.05.061.

Fu, G., A. Heemink, S. Lu, A. Segers, K. Weber, and H.-X. Lin (2016a), Model-based aviation advice on distal volcanic ash clouds by assimilating aircraft in situ measurements, *Atmos. Chem. Phys.*, *16*(14), 9189–9200, doi:10.5194/acp-16-9189-2016.

Fu, G., H.-X. Lin, A. Heemink, A. Segers, F. Prata, and S. Lu (2016b), Satellite data assimilation to improve forecasts of volcanic ash concentrations, *Atmos. Chem. Phys. Discuss.*, 1–22, doi:10.5194/acp-2016-436.

Gudmundsson, M. T., et al. (2012), Ash generation and distribution from the April–May 2010 eruption of Eyjafjallajökull, Iceland, *Sci. Rep.*, *2*, 572, doi:10.1038/srep00572.

Horwell, C., and P. Baxter (2006), The respiratory health hazards of volcanic ash: A review for volcanic risk mitigation, *Bull. Volcanol.*, *69*(1), 1–24, doi:10.1007/s00445-006-0052-y.

Lacasse, C., S. Karlsdóttir, G. Larsen, H. Soosalu, W. I. Rose, and G. G. J. Ernst (2004), Weather radar observations of the Hekla 2000 eruption cloud, *Iceland*, *66*(5), 457–473, doi:10.1007/s00445-003-0329-3.

Le Dimet, F.-X., and O. Talagrand (1986), Variational algorithms for analysis and assimilation of meteorological observations: Theoretical aspects, *Tellus A*, *38A*(2), 97–110.

Leadbetter, S. J., and M. C. Hort (2011), Volcanic ash hazard climatology for an eruption of Hekla Volcano, Iceland, *J. Volcanol. Geotherm. Res.*, *199*(3–4), 230–241, doi:10.1016/j.jvolgeores.2010.11.016.

Lu, S., H. X. Lin, A. W. Heemink, G. Fu, and A. J. Segers (2016), Estimation of volcanic ash emissions using trajectory-based 4D-Var data assimilation, *Mon. Weather Rev.*, *144*(2), 575–589, doi:10.1175/mwr-d-15-0194.1.

Mankin, W. G., M. T. Coffey, and A. Goldman (1992), Airborne observations of SO_2, HC_l, and O_3 in the stratospheric plume of the Pinatubo Volcano in July 1991, *Geophys. Res. Lett.*, *19*(2), 179–182, doi:10.1029/91GL02942.

Marzano, F. S., M. Lamantea, M. Montopoli, S. Di Fabio, and E. Picciotti (2011), The Eyjafjöll explosive volcanic eruption from a microwave weather radar perspective, *Atmos. Chem. Phys.*, *11*(18), 9503–9518, doi:10.5194/acp-11-9503-2011.

Mastin, L. G., M. Guffanti, and R. Servranckx (2009), Alaska Volcano Observatory—A multidisciplinary effort to assign realistic source parameters to models of volcanic ash-cloud transport and dispersion during eruptions, *J. Volcan. Geoth. Res.*, *186*, 10–21.

Mona, L., A. Amodeo, G. D'Amico, A. Giunta, F. Madonna, and G. Pappalardo (2012), Multi-wavelength Raman lidar observations of the Eyjafjallajökull volcanic cloud over Potenza, southern Italy, *Atmos. Chem. Phys.*, *12*(4), 2229–2244, doi:10.5194/acp-12-2229-2012.

Petäjä, T., et al. (2012), In-situ observations of Eyjafjallajökull ash particles by hot-air balloon, *Atmos. Environ.*, *48*, 104–112, doi:10.1016/j.atmosenv.2011.08.046.

Prata, A. J., and A. T. Prata (2012), Eyjafjallajökull volcanic ash concentrations determined using Spin Enhanced Visible and Infrared Imager measurements, *J. Geophys. Res.*, *117*, D00U23, doi:10.1029/2011JD016800.

Rose, W. I., and A. J. Durant (2009), Fine ash content of explosive eruptions, *J. Volcanol. Geotherm. Res.*, *186*(1–2), 32–39, doi:10.1016/j.jvolgeores.2009.01.010.

Rose, W. I., G. J. S. Bluth, D. J. Schneider, G. G. J. Ernst, C. M. Riley, L. J. Henderson, and R. G. McGimsey (2001), Observations of volcanic clouds in their first few days of atmospheric residence: The 1992 eruptions of crater peak, Mount Spurr Volcano, Alaska, *J. Geol.*, *109*(6), 677–694, doi:10.1086/323189.

Schaap, M., R. M. A. Timmermans, M. Roemer, G. A. C. Boersen, P. J. H. Builtjes, F. J. Sauter, G. J. M. Velders, and J. P. Beck (2008), The LOTOS EUROS model: Description, validation and latest developments, *Int. J. Environ. Pollut.*, *32*(2), 270–290, doi:10.1504/ijep.2008.017106.

Schmetz, J., P. Pili, S. Tjemkes, D. Just, J. Kerkmann, S. Rota, and A. Ratier (2002), An introduction to Meteosat Second Generation (MSG), *Bull. Am. Meteorol. Soc.*, *83*(7), 977–992, doi:10.1175/1520-0477(2002)083<0977:AITMSG>2.3.co;2.

Searcy, C., K. Dean, and W. Stringer (1998), PUFF: A high-resolution volcanic ash tracking model, *J. Volcanol. Geotherm. Res.*, *80*(1–2), 1–16, doi:10.1016/s0377-0273(97)00037-1.

Seibert, P. (2000), Inverse modelling of sulfur emissions in Europe based on trajectories, in *Geophysical Monograph Series*, vol. 114, pp. 147–154, AGU, Washington, D. C., doi:10.1029/gm114p0147.

Stohl, A., et al. (2011), Determination of time- and height-resolved volcanic ash emissions and their use for quantitative ash dispersion modeling: The 2010 eyjafjallajökull eruption, in *Atmos. Chem. Phys.*, vol. 11, pp. 4333–4351., doi:10.5194/acp-11-4333-2011

Strunk, A., A. Ebel, H. Elbern, E. Friese, N. Goris, and L. Nieradzik (2010), Four-dimensional variational assimilation of atmospheric chemical data—Application to regional modelling of air quality, in *Large-Scale Scientific Computing, Lecture Notes in Computer Science*, vol. 5910, edited by A. Strunk et al., pp. 214–222, Springer, Berlin.

Stuefer, M., S. R. Freitas, G. Grell, P. Webley, S. Peckham, S. A. McKeen, and S. D. Egan (2013), Inclusion of ash and SO_2 emissions from volcanic eruptions in WRF-Chem: Development and some applications, *Geosci. Model Dev.*, *6*(2), 457–468, doi:10.5194/gmd-6-457-2013.

Vicente, G. A., J. C. Davenport, and R. A. Scofield (2002), The role of orographic and parallax corrections on real time high resolution satellite rainfall rate distribution, *Int. J. Remote Sens.*, *23*(2), 221–230, doi:10.1080/01431160010006935.

Wang, X., et al. (2008), Volcanic dust characterization by EARLINET during Etna's eruptions in 2001–2002, *Atmos. Environ.*, *42*(5), 893–905, doi:10.1016/j.atmosenv.2007.10.020.

Weber, K., J. Eliasson, A. Vogel, C. Fischer, T. Pohl, G. van Haren, M. Meier, B. Grobéty, and D. Dahmann (2012), Airborne in-situ investigations of the Eyjafjallajökull volcanic ash plume on Iceland and over north-western Germany with light aircrafts and optical particle counters, *Atmos. Environ.*, *48*, 9–21, doi:10.1016/j.atmosenv.2011.10.030.

Webley, P. W., T. Steensen, M. Stuefer, G. Grell, S. Freitas, and M. Pavolonis (2012), Analyzing the Eyjafjallajökull 2010 eruption using satellite remote sensing, lidar and WRF-Chem dispersion and tracking model, *J. Geophys. Res.*, *117*, D00U26, doi:10.1029/2011JD016817.

Wen, S., and W. I. Rose (1994), Retrieval of sizes and total masses of particles in volcanic clouds using AVHRR bands 4 and 5, *J. Geophys. Res.*, *99*(D3), 5421–5431, doi:10.1029/93JD03340.

Winker, D. M., Z. Liu, A. Omar, J. Tackett, and D. Fairlie (2012), CALIOP observations of the transport of ash from the Eyjafjallajökull volcano in April 2010, *J. Geophys. Res.*, *117*, D00U15, doi:10.1029/2011JD016499.

Zakšek, K., M. Hort, J. Zaletelj, and B. Langmann (2013), Monitoring volcanic ash cloud top height through simultaneous retrieval of optical data from polar orbiting and geostationary satellites, *Atmos. Chem. Phys.*, *13*(5), 2589–2606, doi:10.5194/acp-13-2589-2013.